Ground-based MFRSR UV-Vis spectral retrievals of Saharan dust absorption at Izaña Observatory

Hiren Jethva[1,2], Nick Krotkov[2], Omar Torres[2], Jungbin Mok[3], Gordon Labow[3], Elena Lind[2], Tom Eck[4,2], Wei Gao[5], George Janson[5], Scott Simpson[5], Darrin Sharp[5], Kathy Lantz[6], Charles Wilson[6], Africa Barreto[7,8], Rosa García[9,7], Sergey Korkin[4,2], David Flittner[10]

[1]Morgan State University, Baltimore, MD, United States
[2]NASA Goddard Space Flight Center, Greenbelt, MD, United States
[3]Science Systems and Applications, Inc., Lanham, MD, United States
[4]University of Maryland, Baltimore County, GESTAR-II, Baltimore, MD, United States
[5]USDA UV-B Monitoring and Research Program, Natural Resource Ecology Laboratory, Colorado State University, Fort Collins, Colorado, USA
[6]Global Monitoring Laboratory (GML), Radiation, Aerosol, and Cloud Division (GRAD), NOAA, Boulder, Colorado, USA
[7]Izaña Atmospheric Research Center (IARC), State Meteorological Agency (AEMET), Santa Cruz de Tenerife, Spain
[8]Group of Atmospheric Optics, University of Valladolid, Valladolid, Spain
[9]TRAGSATEC, Madrid, Spain
[10]NASA Langley Atmospheric Research Center, VA, United States

Correspondence to: Hiren Jethva (hiren.t.jethva@nasa.gov)

Abstract. This paper presents a multi-instrument synergistic technique to retrieve atmospheric dust aerosol columnar effective imaginary refractive index (*k*), single scattering albedo (SSA), and absorption aerosol optical depth (AAOD). The technique combines: (a) aerosol information derived from the narrow field-of-view measurements by filter sun-moon-sky radiometer within the Aerosol Robotic Network (AERONET): spectral aerosol optical depth (AOD) and inversion properties; (b) the total, direct, and diffuse sky irradiance measurements from UV- and Vis-Multifilter Rotating Shadowband Radiometer (MFRSR); (c) trace gas columns from satellite measurements (OMI and OMPS). The approach is demonstrated on the data collected at the Izaña Atmospheric Observatory (IZO), located at an altitude of 2.4 km on Tenerife Island, a unique site for transported Saharan dust column optical properties retrievals due to very clean background condition for calibrating the instrument. This multi-instrument synergy enables consistent column absorption retrievals from ultraviolet (UV) to visible (VIS) wavelengths, while effectively accounting separately for aerosol and gaseous (Ozone-O_3, and Nitrogen Dioxide-NO_2) absorption. The MFRSR on-site calibration procedure relies on observations acquired on cleaner days (AOD<0.1 at 440 nm) to eliminate the observed dependency of the calibration constant on increasing dust aerosol loading due to an inefficient correction for the forward scattering (aureole effect). The retrieval algorithm 1) integrates the temporally collocated AERONET-retrieved particle size distribution and the real part of the refractive index into the radiative transfer simulations, while accounting for the pre-defined spheroidal shape distribution of the dust aerosols, and 2) fits the measured ratio of diffuse to direct-normal irradiance for discrete wavelengths (325 nm to 440 nm) to the pre-calculated, on-the-fly look-up table to retrieve column effective spectral imaginary part of the refractive index. The sensitivity analysis reveals that the uncertainties

in the AERONET spectral AOD (±0.01 at 440 nm ±0.02 at shorter UV wavelengths) and assumed particle shape distribution constitute the dominant source of error, followed by estimated 1% error in the MFRSR-measured diffuse-to-direct irradiance ratios, in the MFRSR-retrieved *k* and SSA. Overall, the combined errors in the derived SSA at all five MFRSR wavelengths generally remain within ±0.03 for AOD larger than 0.4. The derived SSA at 440 nm shows good agreement with AERONET inversions, mostly within ±0.03 for AOD>0.2, and ±0.02 at higher AOD (>0.4). This close correspondence confirms the consistency between the two fundamentally distinct inversion techniques and enhances confidence in the concurrent MFRSR UV wavelength inversions. We present a multi-year (2019-2023) MFRSR Saharan aerosol absorption record revealing enhanced dust absorption at UV wavelengths with noticeable intraseasonal and interannual variabilities, which are indicative of a varying composition of minerals (iron oxides) in the dust. The spectral aerosol absorption effects reduce the amount of surface-reaching UV radiation and slow down tropospheric photochemistry, which can have implications for air quality, human health, and ecosystem dynamics. The ongoing AERONET and MFRSR measurements currently made at the Santa Cruz ground-level site on Tenerife Island will continue to produce a unique, long-term ground-based UV spectral Saharan dust absorption dataset, providing a valuable reference for evaluating space-based UV aerosol absorption retrievals from instruments such as DSCOVR-EPIC, S5P-TROPOMI, and the most recently launched PACE-OCI. In addition to deriving spectral absorption properties, the enhanced sensitivity of UV measurements to the dust spectral absorption, demonstrated with the MFRSR inversion in this work, can be exploited for inferring the mineralogical composition of the dust aerosols, which is critical to improving the dust representation in Earth System Models.

1 INTRODUCTION

Light-absorbing aerosols, by attenuating incoming solar radiation, play a critical role in governing the magnitudes of radiative balance and tropospheric photochemistry, and influence local to regional air quality, thereby human health. In addition, aerosol-cloud interactions, both through in-situ microphysical processes (indirect effect) and radiative coupling (direct effect), further amplify their potential to alter the regional and global climate. The Intergovernmental Panel on Climate Change (IPCC) Sixth Assessment Report (AR6) emphasizes that aerosol absorption, particularly by substances like black carbon and mineral dust, is a significant source of uncertainty in understanding and modeling the Earth's climate system (IPCC 2021, Forster et al., 2021). This uncertainty arises from pronounced variability in aerosol optical and microphysical properties, driven by diverse compositions, as well as a limited availability of high-quality observational datasets.

Since its inception in 1993 at the NASA Goddard Space Flight Center, the ground-based Aerosol Robotic Network (AERONET) has grown into a global network spanning multiple continents and hundreds of sites, encompassing ecosystems affected by biomass burning, desert dust, and urban-industrial activity (Holben et al., 1998). AERONET employs an automated, sun-sky photometer for making direct sun light measurements across a range of wavelengths from ultraviolet (UV-340 nm and 380 nm) to the shortwave near-infrared (SWIR-1640 nm).

The exact combination of optical filters changed somewhat over the years, with the most recent instrument model (CIMEL CE318-T) having center wavelengths at 340, 380, 440, 500, 675, 870, 940, 1020, 1640 nm. Direct sun

measurements for AOD determination are taken at all these wavelengths with the reported AOD at 340, 380, 440, 500, 675, 870, 1020, 1640 nm and water vapor column at 940 nm. Scattered sky radiance measurements are done at 380, 440, 500, 675, 870, 1020, 1640 nm (starting in 2016) and with additional measurements at 340 nm starting in July 2025 after instrument calibration using CE318-T model and new operational instrument firmware. Current V3 AERONET processing inversion algorithm applies only four key wavelengths (440, 670, 860, 1020 nm) to retrieve aerosol optical and microphysical properties, including, spectral single-scattering albedo (SSA), aerosol particle size distribution (PSD), and aerosol phase function (Dubovik et al., 2002; Sinyuk et al., 2020). Although AERONET makes AOD measurements at 340 nm and 380 nm wavelengths, the sky measurements, essential for aerosol absorption inversion, were made only at 380 nm starting 2016. Due to calibration uncertainties, however, 380-nm sky observations have not been used in the AERONET inversion. This leaves the near-UV spectral region currently devoid of aerosol absorption properties in the V3 database. However, plans are underway to incorporate the past (380 nm) and new (340, 380 nm) UV sky measurements in the upcoming AERONET V4 processing. Extraterrestrial "direct sun" signal calibration of the AERONET reference instruments ("sun masters") is done at high altitude remote sites (Izaña and Mauna Loa Atmospheric Observatories) using the Langley extrapolation analysis. This results in a very high AOD accuracy of ~0.002 in the visible and near infrared to ~0.009 in the UV (Eck et al, 1999) for the sun masters.

Since the launch of NASA's Earth Observation System (EOS: https://science.nasa.gov/earth-science/the-earth-observer/) program in the 1990s, tremendous progress has been made in characterizing the global distribution of aerosol optical and microphysical properties from a suite of satellite sensors having unique capabilities. These include active and passive sensors, multiangle imagers, and UV to VIS to SWIR spectral coverage. Among them, the Ozone Monitoring Instrument (OMI) on board the Aura satellite stands out as the only sensor to provide a two-decade long aerosol absorption record in the near-UV spectral region (Torres et al., 2007; Torres et al., 2018). The two-channel near-UV algorithm applied to OMI, and later extended to Deep Space Climate Observatory Earth Polychromatic Camera (DSCOVR-EPIC) taking global "snapshot" measurements of the entire sun-lit Earth Disc from Sun-Earth Lagrange 1 orbit every 1-2 hours and Low Earth Orbit Sentinel Precursor (S5P-TROPOMI) sensors, takes advantage of the enhanced sensitivity of the top-of-atmosphere (TOA) observations at UV wavelengths to aerosol absorption and retrieves AOD and SSA simultaneously at 388 nm. The evaluation of the SSA retrievals from these spaceborne sensors relied on extrapolation from the near-UV 388 nm to 440 nm to facilitate a direct comparison against AERONET inversion (Jethva et al., 2014; Torres et al., 2020; Ahn et al., 2021). The current lack of AERONET ground-based inversions of aerosol absorption at UV wavelengths restricts a direct evaluation at the satellite retrieval wavelength.

The SKYNET network, a ground-based radiometric observation system with sites across Asia and Europe, conducts automated spectral measurements of direct solar flux and sky radiances. These observations are used in inversion algorithms to derive spectral AOD and SSA across the near-UV to NIR spectral range (Nakajima et al., 1996; Hashimoto et al., 2012). The availability of the SKYNET SSA inversion dataset in the UV spectrum enabled, for the first time, a direct evaluation of OMI-derived SSA at UV wavelengths, thus eliminating the need for spectral extrapolation to visible wavelengths as required in AERONET-based evaluations (Jethva et al., 2019). However, a

key limitation of SKYNET's inversion approach is its assumption of a fixed, spectrally neutral surface albedo (set at 0.1) across UV to visible wavelengths (Campanelli et al., 2015), which can lead to underestimation of SSA, particularly under low aerosol loading conditions (Mok et al., 2018). While SKYNET data proved valuable for assessing OMI aerosol absorption products, the study was constrained to a limited number of sites, primarily in Asia and Europe.

The UV-Vis Multifilter Rotating Shadowband Radiometer (UV-VIS MFRSR) (Harrison et al., 1994) is a unique addition to the existing ground network for surface UVB irradiance (https://uvb.nrel.colostate.edu/UVB/) and aerosol monitoring (Michalsky et al., 2001). The modified version of the MFRSR instrument makes 1-minute measurements of total hemispheric and diffuse hemispheric spectral downwelling planar irradiance measurements at five UV wavelengths (311, 325, 332, 340, 380 nm) and a single visible (440 nm) wavelength (Krotkov et al., 2005a; Mok et al., 2016, 2018). The SSA inversion research algorithm developed and demonstrated by Krotkov et al. (2005b) uses these measurements, in synergy with the collocated direct AOD and inversion dataset from AERONET, to fit the observed diffuse-to-direct ratio measurements to the on-the-fly radiative transfer (RT) simulations to derive the imaginary part of the refractive index independently at 440 nm and UV wavelengths, except 311 nm.

The two modified UV-VIS MFRSR sensors were deployed at the AERONET calibration site at NASA Goddard Space flight Center in Maryland since 2005 and participated in several pollution targeted field campaigns in Santa Cruz, Bolivia in September-October 2007 (Mok et al., 2016), Mexico City during MILAGRO campaign in March 2006 (Corr et al., 2009), and , from April to August 2016 in Seoul, South Korea, to study urban pollution aerosols, including transported Asian dust (Mok et al., 2018). A combination of AERONET, MFRSR, and Pandora (AMP) retrievals provided aerosol absorption data across UV-B (305 nm) to NIR (870 nm) wavelengths, isolating aerosol and gaseous absorption (e.g., NO_2, O_3). These findings underscore the significance of multi-instrument analysis for measuring spectral aerosol absorption properties in the UV and VIS wavelengths for climate, photochemistry, and health studies. For example, measuring biomass burning aerosols in Amazon Basin during 2007 Bolivia campaign our UV-MFRSR measurements revealed that brown carbon (BrC) exhibits enhanced UV absorption, which reduces available surface UV-B radiation (290-320 nm) and slows the rate of tropospheric photochemical reactions (Mok et al., 2016). This resulted in simulations of decreased ozone production and reduced radical concentrations (OH, HO_2, RO_2), thereby mitigating some adverse effects of biomass-burning emissions.

Starting in July 2019, a new UV-VIS MFRSR instrument (head # 582) was deployed at the Izaña Atmospheric Observatory (IZO) at an altitude of ~2.4 km above the sea-level in Tenerife Island located at about 350 km northwest from the western coast of the Saharan Desert (see Figure 1). The instrument was in near-continuous operation until October 2023 and collected valuable spectral sun and sky irradiance measurements at five discrete UV (311, 325, 332, 340, 380 nm) and visible (440 nm) wavelengths. Prior to the deployment at the Izaña Observatory, the MFRSR instrument was calibrated at the NOAA Central UV Calibration Facility (CUCF) to accurately characterize its radiometric, spectral and angular responses. Figure 2 shows the spectral response function, central wavelength (CW), wavelength range, and full-width-half-maximum (FWHM) of five bands of MFRSR head # 582 used in the present

work. Table 1 lists the MFRSR and AERONET datasets employed in the present synergistic aerosol absorption algorithm.

In this work, we present a multi-year inversion record of UV-VIS spectral aerosol absorption retrieved from the MFRSR direct and diffuse irradiance measurements acquired at IZO. Section 2 describes the MFRSR instrument characteristics and calibration procedure. Section 3 presents the spectral absorption retrieval algorithm. The uncertainty estimates of the retrieved spectral imaginary part of the refractive index and SSA are presented in Section 4. Section 5 discusses the results, including the SSA retrievals at 440 nm and their comparison against those of AERONET, a multi-year inversion record of UV to VIS SSAs, and spectral characteristics of dust aerosol absorption. Section 6 summarizes the work and its future implications in the evaluation of satellite aerosol absorption retrievals.

2 MFRSR On-site Calibration Procedure

In this section, we describe a new, on-site MFRSR calibration procedure involving three steps that requires AERONET-measured spectral AODs, along with Rayleigh and trace gas absorption optical depths, to derive the top-of-atmosphere (TOA) calibration constant V_0 [milli-volts] that would have been measured by the MFRSR at the TOA. The improved calibration procedure at the IZO site has an additional step 2, compared to the previously adopted procedure for fine-mode particles (Krotkov et al. 2005a). This new step 2 corrects the direct and diffuse irradiances measured during dust events for the sun forward scattering (aureole) effect, which is necessary for large, coarse-mode particles (dust) and larger AOD.

2.1 Step 1: Calculations of Calibration Constant V_0 on Cleaner Days

The calibration procedure starts with identifying the mostly aerosol-free, cleaner days with an AERONET measured AOD (440 nm) < 0.1. The MFRSR instrument measures raw total (full hemispheric view) and diffuse (sun shadowed) voltages [milli-volts] near-simultaneously for seven narrow filter (solid state detector) channels every minute. There are 2 additional voltage measurements with the shadow band blocking the sky radiance in aureole directions on each side of the sun. These measurements are used to correct for the forward scattered solar light around the sun (aureole) (Harrison et al., 1994). The complete cycle takes ~10 sec and is repeated every 1 minute throughout the day. For on-site MFRSR calibration, we use spectrally and time interpolated AERONET level 1.5 extinction aerosol optical depths, $\tau_{AER}(\lambda_{rad})$, where λ_{rad} is the radiatively equivalent wavelength for each channel (Krotkov et al., 2005a). The surface pressure adjusted scattering molecular optical depth (i.e., Rayleigh OD, $\tau_{Ray}(\lambda_{rad})P$) and the absorption optical depths of trace gases (O_3 and NO_2) are also computed at λ_{rad} using satellite or co-located ground-based (e.g., PANDORA) trace-gas column measurements. The total atmospheric column extinction optical depth is then multiplied with the direct-sun air-mass factor, $sec(SZA)$, where SZA is solar zenith angle and combined with the cosine-corrected direct-normal voltage measurement, V_{dirn}^{Meas}/f_R, to calculate the calibration constant (V_0^{Clean}) for each channel and measurement cycle throughout the day, as formulated in Equation (1):

$$\ln(V_0^{Clean}) = ln(V_{dirn}^{Meas}/f_R) + sec(SZA) \times \left[\boldsymbol{\tau_{AER}(\lambda_{rad})} + \tau_{Ray}(\lambda_{rad})P + \tau_{gas}(\lambda_{rad})\right] \quad (1)$$

τ_{AER} is interpolated with a 2nd order polynomial from 4 AERONET direct sun level 1.5 AOD (340 nm, 380 nm, 440 nm, 500 nm) in log-log space to λ_{rad} (Eck et al. 1999); τ_{Ray} is the Rayleigh optical depth adjusted to the atmospheric pressure, f_R is the laboratory-measured and cosine-normalized angular response (*i.e.*, see fig. 4 in Krotkov et al, 2005a), and τ_{gas} is the combined optical depth of the trace gases of Ozone (O_3) and NO_2 obtained from Aura/OMI sensor for almost entire record, except for the last three months (July through September 2023) during which the total O_3 column densities retrieved from SNPP-OMPS were used. Additionally, the O_3 and NO_2 amounts measured from the collocated ground-based Pandora instrument were used, whenever available, during the same period. Note that all radiative transfer calculations accounting for the Rayleigh, gaseous, and aerosol atmospheres were carried out at the radiatively equivalent wavelength λ_{rad} calculated for each measurement and spectral channel, as shown in Krotkov et al. (2005a). Figure 3 shows examples illustrating the Step 1 of the calibration procedure for clean days on August 20 and 31, 2020, when AERONET-measured AOD at 440 nm (AOD_{440}) were less than 0.03. The true-color RGB image captured by the MODIS sensor onboard the Aqua satellite visually confirms no dust transport from the Saharan desert on these two dates. The natural logarithm of V_0, $ln(V_0)$, calculated from equation (1) for each 1-minute measurement is shown on the left-hand y-axis as red-green-blue-black dots. The different colors show the effect of the iterative removal of outlier measurements with V_0 values outside of 3σ standard deviation. The final selections (182 and 184 retained measurements out of original 209 and 211) are shown as black dots, while the black horizontal lines show the daily average $< ln(V_0) >$ values. The red lines show independent Langley intercept calibrations applied to all filtered MFRSR morning measurements between 8 and 12 UTC (black dots). There is excellent agreement with the AERONET-based calibration on August 31 when the AOD remained approximately constant. On August 20, the Langley intercept is 1% lower than the AERONET-based $< ln(V_0) >$ because the AOD systematically increased during the morning Langley calibration period. We do not use Langley calibrations in this work.

Equation (1) was applied to all 1-minute MFRSR morning measurement cycles between 8 and 12 UTC resulting in (after removing outliers using an iterative procedure that discards data points outside 3σ standard deviation) a daily average $< \ln(V_0^{Clean}) >$ value of 8.111 and 8.116 on the respective dates. An increase in V_0 by 0.5% from August 20 to 31 is real and attributed to the reduction in the Sun-Earth distance between the two dates. The Step 1 procedure described above was applied to each MFRSR spectral channel for a total of the 223 cleanest days with an AOD_{440}<0.10 identified during the AERONET-MFRSR combined operation period 2019-2023.

2.2 Step 2: Direct Voltage Correction on Dusty Days

Equation (1) can be inverted to calculate MFRSR aerosol optical depth: $\tau_{MFRSR}(\lambda_{rad})$ assuming known daily average calibration constant (i.e., $< \ln(V_0^{Clean}) >$), which can be estimated either from Langley intercept (Harrison and Michalsky, 1994) or using our Step 1 calibration procedure. For days with low AOD or fine-mode dominated aerosols (e.g., smoke, Mok et al., 2016), the MFRSR-derived and AERONET measured AOD typically agree within estimated uncertainties, e.g., $|\tau_{AER} - \tau_{MFRSR}| < 0.01$ for AOD < 0.5 (Krotkov et al., 2005a). However, for dusty days with large AOD dominated by coarse mode aerosols, the V_{dirn}^{Meas} becomes overestimated due to under corrected aureole effect. On the other hand, AERONET direct sun AOD measurements $\tau_{AER}(\lambda_{rad})$ are much less affected by the aureole effect even for coarse dust particles due to CIMEL small field-of-view (~1.2°). Therefore, we calculate corrected

direct-normal voltages, V_{dirn}^{Corr} on dusty days with AERONET $AOD_{440} > 0.2$ using equation (2) and the median of the cleaner day calibration constants during each month, $< V_0^{Clean} >_m$:

$$\ln(V_{dirn}^{Corr}) = ln(< V_0^{Clean} >_m) - sec(SZA) \times \left[\boldsymbol{\tau_{AER}(\lambda_{rad})} + \tau_{Ray}(\lambda_{rad})P + \tau_{gas}(\lambda_{rad})\right] \quad (2)$$

2.3 Step 3: Diffuse Voltage Correction on Dusty Days

In the final calibration step, the corrected diffuse voltage, V_{dif}^{Corr}, is calculated by subtracting the corrected direct horizontal voltage, V_{dirn}^{Corr}, from the cosine-corrected measured total voltage, $\frac{V_{Total}^{Meas}}{fT}$, as given in Equation 3:

$$V_{dif}^{Corr} = \frac{V_{Total}^{Meas}}{fT} - cos(SZA)V_{dirn}^{Corr} \quad (3)$$

Where f_T is the effective cosine correction factor applied to the total (direct plus diffuse) raw irradiance measurement (Krotkov et al., 2005a). Figure 4 illustrates the Step 2 and Step 3 of the calibration procedure for August 26, 2020. The three-step calibration procedure described above yields the corrected diffuse voltage, V_{dif}^{Corr} for dusty day observations. Note that while the partition between direct and diffuse irradiance is adjusted according to Eq. (2) and Eq. (3), the total voltage V_{Total}^{Meas} measured by MFRSR does not change in the calibration process. The dimensionless ratio of the corrected diffuse to corrected direct-normal irradiance is then used in the retrieval algorithm to retrieve the imaginary part of the complex refractive index for each 1-minute measurement on dusty days with $AOD_{440} > 0.2$.

3 Aerosol Absorption Inversion Algorithm

The MFRSR inversion procedure involves several steps, beginning with creating a matchup file of the temporally collocated AERONET direct and inversion measurements, simulating the phase matrix of spheroidal dust aerosols, performing RT simulations of downward surface-reaching direct and diffuse irradiance, and finally applying a direct fit between the measurements and simulations.

3.1 Description of the RT model

We employ a Gauss–Seidel radiative transfer model, formally referred to as the Arizona RT model, for simulating the at-surface spectral direct and diffuse downwelling planar irradiances. The 1-dimensional RT code accounts for gaseous absorption as well as molecular and aerosol multiple scattering (Herman and Browning, 1965). In this plane-parallel atmosphere, sphericity is included in the incoming solar beam, also known as the pseudo-spherical approximation (Caudill et al. 1997). The model creates a total of 100 vertical atmospheric layers with associated molecular, aerosols, and input trace gases profiles. Absorption cross-sections of ozone and nitrogen dioxide are averaged for each channel using the appropriate bandwidths to derive effective absorption layer optical depths at λ_{rad} values used in the RT model. The reflecting surface is modeled as Lambertian with albedo obtained from AERONET Level 1.5 inversion at 440 nm, which also is used at all MFRSR UV channels. The aerosol absorption inversion procedure begins with the availability of the AERONET Level 1.5 direct measurements of spectral AOD and inversion

parameters of particle size distribution and the real part of the refractive index (n). Each instance of an MFRSR measurement was temporally collocated with the AERONET direct sun AOD measurements within ±15 minutes and available closest-in-time inversion products on a daily basis. Note that, no averaging was performed on the MFRSR measurements. Instead, all 1-minute MFRSR measurements were assigned to the corresponding collocated AERONET parameters. For each instance of AERONET-MFRSR collocated points, the spectral AODs in the range 340-500 nm are used to derive a quadratic relationship between AOD and wavelengths in log-log space, which then was used to estimate the AOD at the MFRSR radiatively equivalent channel wavelength λ_{rad}.

3.2 Spheroidal Shape Treatment of Dust Aerosols

The Izaña Observatory in the Tenerife Island is located in the northwest pathways of long-range dust transport from the Sahara Desert. During such transport events, the mineral dust from the Sahara constitutes the major component of aerosols over the region. Sea salt and locally emitted aerosols might also contribute to the total loading although their contribution is minimal as evident from the very low AOD_{440} (<0.05) measured by the AERONET on dust-free, cleaner days. Outside the dust transport season (Jun, July, August), Izaña is predominantly under background clean conditions the rest of the year as a consequence of the prevailing westerly flows of the North Atlantic free troposphere at subtropical latitudes, with subsequent transatlantic transport of North American dust, non-sea-salt sulfate and organic matter as main contributors (García et al., 2017, Barreto et al., 2022). Since the focus of the present study is to retrieve spectral aerosol absorption of the transported Saharan dust particles, the mineral dust aerosol is assumed to be the sole component of the aerosol loading.

Dust aerosols are known to be non-spherical in shape, as shown by several studies (Dubovik et al., 2006; Torres et al., 2018). A satellite-based retrieval study, based on the Aura-OMI observations, has shown that assuming spherical dust particles produces large biases in the retrieved AOD (388 nm) between the two sets of scattering angle geometries, i.e., forward and back scattering, over the semi-arid region of Sahara. These results created the necessity to modify the dust aerosol model used in the OMI near-UV aerosol retrieval algorithm.

Accurate representation of the scattering phase function of large non-spherical particles, such as dust aerosols, requires numerical tools such as T-matrix theory (Waterman, 1971; Bohren and Singham, 1991; Mishchenko and Travis, 1994), geometric optics (Yang and Liou, 1996) or a combination of the two approaches (Dubovik et al., 2006). The simplest and most commonly assumed non-spherical shapes for which exact analytical solutions can be obtained are spheroids characterized by their aspect or axis ratio (ε). While the T-matrix theory applied to the spheroidal shape particles reproduces the laboratory measurements of the scattering phase function significantly better than spheres, it breaks down for highly elongated spheroids of a very large size parameter (Mishchenko et al., 1997). The geometric optics method, on the other hand, documented in Yang et al. (2000) accurately accounts for scattering effects of spheroids of aspect ratios and size parameters beyond the range handled by the T-matrix theory. Dubovik et al. (2006) blended the advantages of the T-matrix theory and Geometric Optics method to create a set of pre-calculated look-up tables (LUT) of phase matrix elements of randomly oriented spheroids at a 1 degree scattering angle resolution. The associated software package, formally referred to as the Light Scattering Simulations (or popularly referred to as DLS

package within the aerosol community), handles a wide range of the real part of the refractive index (1.33-1.6), the imaginary part of the refractive index (0.0005-0.5), aspect ratios (0.3-3.0), and size parameters (0.012-625). Using this package, Torres et al. (2018) simulated the phase matrix elements for the dust aerosol models used in their satellite Aura Ozone Monitoring Instrument (OMI) UV aerosol retrievals (OMAERUV). The aspect ratio distribution assumed in the OMAERUV calculations was taken from Dubovik et al. (2006), which is shown as the black curve in the inset plot of Figure 5 (a).

Torres et al. (2018) demonstrated that using a near-UV aerosol lookup table (at 354 nm and 388 nm), based on phase matrix elements derived from spheroidal aspect ratios proposed by Dubovik et al. (2006), significantly reduced scan bias in the OMI AOD retrievals. This approach improved consistency between retrievals on the west side (characterized by lower backscattering or forward-scattering angles) and the east side (backscattering angles) of the OMI scan over the Saharan Desert. The improvements in the OMI AOD retrievals reflect the effectiveness of the assumed spheroidal aspect ratio distribution over the dust source region. A similar analysis for the Saharan dust transport over the Atlantic Ocean post Torres et al. (2018) publication, however, still showed asymmetry in the retrieved AOD between the East and West sides of the OMI swath. These results necessitated testing different spheroidal distributions to investigate their impacts on the dust AOD retrievals. Three distinct aspect ratio distributions reflecting different adjusting weighting factors were used individually in the OMI-based near-UV aerosol retrievals over ocean. The adjustment in weighting factors between these three distributions was made empirically, while constraining the sum of all factors to be 1.0, by gradually increasing the contribution of spherical particles. The aerosol look-up tables created using the three corresponding sets of phase matrix elements generated using original DLS software tool were used in the OMI aerosol algorithm to investigate the retrieval results. We found that the final set of aspect ratios, characterized with a continuous distribution of weighting factors as a function of axis ratio bins with greater weights given to spherical particles, shown as the red curve in the Figure 5(a), largely eliminated the observed asymmetry in the OMI dust AOD retrievals over the Atlantic Ocean. Supplementary Figure 1 illustrates the timeseries of monthly mean OMI AOD [388 nm] for the Atlantic Ocean comparing retrievals from westside and eastside of scan derived assuming spheroidal and empirical aspect ratios models. The summertime (June-Juy-August) global distribution of OMI dust AOD derived separately from the data collected on the west and east sides of the scan are presented in Supplementary Figure 2. Although these results were not previously published, they were adopted for over-ocean dust aerosol AOD and SSA operational retrievals using near-UV observations by the OMI and TROPOMI sensors (Torres et al. 2020), and EPIC-DSCOVR measurements (Ahn et al. 2021). The over-land dust AOD/SSA retrievals from these sensors still use the original spheroidal aspect ratio distribution proposed in Dubovik et al. (2006). The weighting factors distribution parameter as a function of radius for randomly oriented spheroids proposed in Dubovik et al. (2006) and those used in the over-ocean aerosol retrievals from near-UV sensors are listed in Table 3.

Figure 5 shows the scattering phase function F11 for the 440 nm wavelength for a single set of MFRSR-AERONET collocated measurements of mineral dust aerosols acquired on a) August 26 at 10:10 UTC, b) August 27 at 10:19 UTC, and c) August 28 at 15:09 UTC of 2020 corresponding to randomly oriented spheroids proposed in Dubovik et al. (2006) (black), empirically derived distribution (red) used in the present study, and that from AERONET inversion

product (blue). F11 (except retrieved from AERONET) was simulated using the refactored DLS software package (named as the API and described in Appendix). The differences in F11 between the two aspect ratio distributions are quite small for scattering angles smaller than 120°. However, they deviate increasingly at large scattering angles, where the use of the randomly oriented spheroidal model of Dubovik et al. (2006) produces substantially lower F11 values than the empirically derived aspect ratio distribution representing a mixture of spheroids and spheres. Despite these differences, the corresponding SSAs (black and red) show a close agreement—indicating that the choice of aspect ratio distribution didn't play a significant role in the inversion for these three dust events. A sensitivity analysis quantifying the change in the derived SSA due to different dust shape factor distributions is presented in section 4 and also included in Table 4.

The aspect ratio distribution of the Saharan mineral dust inferred from electronic microscope and in situ measurements as reported in the published literature shows a great deal of variability. Ried et al. (2003) sampled the African dust during the Puerto Rico Dust Experiment and found dust to have a significantly higher aspect ratio near 1.9 with standard deviation of 0.9 after long-range transport. Huang et al. (2020) compiled the aspect ratio of the mineral dust aerosols representative of the Saharan and Asian deserts published in the literature, and showed a trend of increasing aspect ratios for northern African dust after transatlantic advection. Specifically, the median aspect ratio increased from 1.60 ± 0.07 in the dust source regions of North Africa to 1.66 ± 0.03 for short-range transported dust and 1.90 ± 0.04 for long-range transported dust. This increase in particle non-sphericity or aspect ratio during transport is attributed to the preferential settling of spherical particles, which have a greater terminal fall speed than aspherical particles of the same volume. Overall, the aspect ratios reported for North African dust were in the range 1.4-2.0.

More recently, Panta et al. (2023) reports high non-sphericity of dust particles collected during the FRontiers in dust minerAloGical coMposition and its Effects upoN climaTe (FRAGMENT) field campaign in the Moroccan Sahara in September 2019, with mean and median aspect ratios of ~1.55±0.38 and 1.46, noting that it does not vary strongly with particle diameter. Aryasree et al. (2024) found that the aspect ratio of the Saharan air layer measured at the Capo Verde and Caribbean sites did not change significantly and remained in the range 1.5-2.0.

Accurately representing the true aspect ratio distribution of dust airmass observed by the MFRSR during absorption inversion at the study site remains a challenging problem. As a first approximation, we adopted an empirically derived model previously used in satellite-based Aura/OMI AOD retrievals in UV. It is important to note that improved aerosol retrievals from satellite observations do not necessarily confirm the presence of a mixture of spherical and spheroidal particles. Rather, this improvement suggests that such a mixture best reproduces the observed solar backscattered UV (BUV) radiances, even though real dust particles are typically angular and irregular, not smooth and spheroidal as represented in the model. Driven by the improved OMI AOD retrievals over land and ocean using two distinct models of spheroidal aspect ratio distribution, the over-ocean dust retrievals in the near-UV aerosol algorithm applied to OMI (Torres et al., 2018), S5p-TROPOMI (Torres et al., 2020), and DSCOVR-EPIC sensors (Ahn et al., 2021) was also updated.

Both AERONET and satellite retrieval algorithms assume spheroidal particle shapes primarily because: (1) computationally efficient scattering algorithms for irregularly shaped particles are not readily available, and (2) the spheroidal approximation captures some of the key scattering phase matrix angular features of randomly oriented desert dust particles reasonably well. More importantly, in the context of this study, incorporating these empirically derived aspect ratios into the aerosol LUT significantly improved the agreement in SSA at 440 nm between MFRSR and AERONET inversions. The results of such comparison on a much larger retrieval dataset are discussed in Section 5.1.

During the summer months, the Izaña observatory on Tenerife Island observes transported dust that originated in the Saharan Desert. Although suspended dust particles are complicated in shape and size that are practically difficult to model in RT simulations, we hypothesize that the dust airmass measured at the site is composed of a mixture of spheres and spheroidal particles for the reasons explained above. The phase matrix associated with the adopted empirically derived aspect ratio distribution was simulated using a modified, substantially faster version of the Light Scattering DLS package for all RT calculations (Lyapustin et al., 2021; Korkin and Lyapustin 2023). See Appendix for a detailed description of how the original DLS package was modified with a specific aim to shorten the computational time without losing accuracy. A test performed to evaluate the differences in the simulation between the original and refactored DLS software tools revealed minor differences of ~0.001-0.002 in the simulated SSA for the dust aerosol inversion measurements at the Izaña site. Such small differences in the SSA simulations are negligible compared to the expected uncertainties in the spectral SSA due to the uncertainties in the measurement calibration and other assumptions made in the inversion procedure.

3.3 MFRSR-AERONET MATCHUP PROCEDURE

The matchup procedure of the AERONET-MFRSR measurements deals with the three kinds of datasets: 1-minute MFRSR measurements of diffuse and direct-normal voltages, AERONET Level 1.5 almucantar combined with hybrid sky scan inversion dataset, and AERONET Level 1.5 direct spectral AOD measurements. While the AERONET Level 1.5 almucantar scans are mostly performed during the early morning-late afternoon hours, ensuring an adequate sky signal at higher solar zenith angles (>50°), hybrid scans are made once per hour throughout the day. Direct measurements of spectral AOD are made typically at 5-minute intervals at the Izaña site. To maximize the usage of the MFRSR's 1-minute hemispheric sky observations, each of these measurements were temporally collocated with the nearest available AERONET inversion instance, either almucantar or hybrid, within a specific day. For instance, near-noon MFRSR measurements could be matched with either morning or afternoon AERONET inversion data, whichever is closest in time. Similarly, the nearest-in-time direct AERONET AOD measurements were also assigned to each MFRSR data points. This simple temporal collocation procedure provided a matchup dataset which begins with an instance of the AERONET inversion dataset (the real and imaginary part of the refractive index, particle size distribution, and other related parameters) followed by a number of collocated MFRSR measurements that include diffuse and direct-normal voltages and corresponding AERONET spectral AODs. This procedure was performed for each wavelength of the MFRSR independently.

3.4 PROCEDURE FOR AEROSOL ABSORPTION INVERSIONS

The MFRSR-AERONET merged file contains each instance of the AERONET direct and inversion data product values and a corresponding number of collocated MFRSR 1-minute measurements for a specific day. For the 440-nm wavelength measurements, the real and imaginary parts of the refractive index and the particle size distribution parameters provided by AERONET were used to create input files for the refactored DLS (the API) package. A total of 21 bins of aspect ratio distribution ranging from about 0.4 (oblate) to about 2.5 (prolate) are prescribed with associated weighting factors shown as the red curve in Figure 5(a). The AERONET volume size distribution defined at fixed 22 radii bins was used as direct input to the API. Using these parameters as input, the phase matrix elements were simulated at a total of 181 scattering angles at a 1-degree resolution. The resultant phase matrix values along with the total AOD measured by AERONET and trace gas absorption optical depths were then ingested into the ARIZONA RT code to simulate the diffuse and direct surface irradiance at the prescribed atmospheric pressure. The vertical profile of aerosols is assumed to follow the Gaussian distribution with the peak concentration at 3 km above ground.

We adopted a look-up table-based approach in which the simulation of the ratio of diffuse to direct-normal (DD) irradiance was created using the phase matrix calculated for a total of 15 node values of the imaginary part of the refractive index. The measured diffuse to direct ratio was then fitted linearly to an array of simulations to derive the imaginary part of the refractive index and SSA. The Jacobians quantifying the sensitivity of the retrieved imaginary part of the refractive index to the simulated DD ratio and the SSA to the imaginary part of the refractive index were also calculated. These Jacobians are useful to estimate uncertainty in the derived SSA due to prescribed uncertainty in the DD ratio measurements. The entire inversion procedure was applied to each of the five wavelengths of the MFRSR independently.

The aerosol absorption inversion procedure described above essentially follows the method described in Krotkov et al. (2005b), except that 1) the aerosol phase matrix for the coarse mode dust aerosols is simulated externally and ingested into the ARIZONA RT model instead of using the Mie theory calculations for spherical particles, and 2) adoption of a LUT-based approach to find the solution in the imaginary part of the refractive index, which is more efficient than an original iterative procedure, which fails for certain observations. A simplified flowchart of the AERONET-MFRSR synergistic algorithm is illustrated in Figure 6.

The entire MFRSR multi-wavelength observations record at IZO was processed with the present algorithm. The inversions were attempted for all observations at all five wavelengths with $AOD_{440} > 0.2$ and solar zenith angle < 70°. "Successful" retrievals are defined as those in which both k and SSA are derived for each 1-minute MFRSR observation at a given wavelength independently of other wavelengths. If a retrieval fails at one wavelength but succeeds at others, the successful results are not discarded but retained and reported for the corresponding wavelengths. Consequently, the number of successful retrievals may vary across wavelengths. Table 2 lists the total number of processed observations and valid inversions performed for different wavelengths and years. It was noticed that the inversion success rate for the 440-nm wavelength is noticeably lower compared to other shorter wavelengths. The majority of these failed retrieval attempts corresponds to either lower AOD conditions ($0.2 < AOD_{440} < 0.4$) and/or

larger solar zenith angles (65°-70°), and higher AERONET SSA (440 nm) of ~0.98. Under such conditions and at the minimum node value of 0.0005 in the imaginary part of the refractive index, the measured DD ratios, even after accounting for 1% uncertainty in the measurements, were found to be significantly higher compared to the RT simulations at the minimum node value of 0.0005 in the imaginary part of the refractive index, below which DLS simulations are not recommended. Another source of uncertainty in retrieving aerosol properties at lower AOD conditions at the Izaña site is the lower boundary reflectance with bi-directional reflectance distribution function (BRDF) of the mountain slope. Additionally, clouds and the Rayleigh-aerosol radiative interactions from the atmosphere below the station can also modify the spectral sky radiance measured by both MFRSR and AERONET sensors. Accounting for these effects in the inversion algorithm is complicated, which makes retrievals on higher altitude mountain slope stations more complicated, difficult, and uncertain than those at stations with relatively a flat surrounding landscape/terrain.

4 UNCERTAINTY CHARACTERIZATION

One of the primary inputs to the present synergy algorithm is the AERONET-measured AOD, which is known to be accurate to within +/-0.01 and +/-0.02 at the at 440 nm and shorter UV wavelengths, respectively, primarily arising due to calibration uncertainty (Eck et al., 1999; Sinyuk et al., 2020). Consequently, the stated error in the spectral AOD used as a constraint in the aerosol absorption inversion, therefore, can produce proportional errors in the retrieved imaginary part of the refractive index *k* and SSA. Another source of uncertainty arises from the absolute error in the measured diffuse-to-direct irradiance ratio, estimated to be approximately ~1%. Additionally, the monthly median value of the calibration constant, ln(V0), calculated on the cleaner days (AOD440<0.10), is applied to all dusty day inversions in a given month, introducing an additional source of error in the absorption inversion. Since the diffuse-to-direct irradiance ratio is used as a measurement matrix and fitted to the RT calculations, its dependence on the absolute value of calibration constant is reduced.

To estimate the uncertainties in the retrieved *k* and SSA associated with these error sources, the inversion algorithm was applied three times to each 1-minute MFRSR measurements using the unperturbed and perturbed AERONET AOD values by +/-0.01 and +/-0.02 at 440 nm and shorter UV wavelengths, respectively. The resulting perturbed retrievals were then compared against unperturbed retrievals to quantify the sensitivity of *k* and SSA to changes in AOD. Separately, Jacobians quantifying the change in the retrieved *k* and SSA with respect to simulated diffuse-to-direct ratio were computed for each valid retrieval to calculate the uncertainty associated with 1% error in the measured DD ratio.

Figure 7 presents the error estimate of *k* for each MFRSR wavelength, shown as box-and-whisker plot, as a function of coincident AERONET spectral AOD. The orange and blue boxes represent errors resulting from perturbing the AOD by +/-0.01 at 440 nm and +/-0.02 at UV wavelengths, respectively. The filled green circles indicate errors incurred by 1% perturbation in the measured DD ratio. At all wavelengths, the errors are found to decrease monotonically with increasing AOD, with largest errors of ~ +/-0.002 at 440 nm and +/-0.004 at UV wavelengths occurring at lower AOD range 0.2-0.4. A decrease (increase) in AOD by 0.01 or 0.02 results in a decrease (increase)

in the retrieved *k*. Errors in **k** caused by a 1% change in the DD ratio are substantially smaller (<0.001) than those induced by AOD perturbations, particularly at low AOD.

Errors in the derived SSA, as displayed in Figure 8, show an opposite behavior: negative (positive) perturbations lead in increased (decreased) SSA. At lower AOD values (0.2-0.4), SSA errors at 440 nm are typically within +/-0.03, but can reach as high as +/-0.06 at UV wavelengths. However, the errors greatly reduce at AOD>0.4 and remain within +/-0.03 or lower even at UV wavelengths. A 1% perturbation in the measured DD ratio contributes relatively minor additional uncertainty, producing SSA errors of roughly 0.01 at AOD < = 0.4 and even smaller errors at higher AOD.

The error estimation was further extended by accounting for the perturbation in the assumed aerosol layer height. The vertical profile of dust aerosols is assumed to follow a Gaussian distribution with peak concentration at 3 km above ground and half width of 0.5 km. The synergy inversion algorithm was applied to three representative dust cases observed on August 26, 27, and 28 of 2020, with the aerosol layer height perturbed by ±1 km from the assumed 3 km. For the higher AOD case on 26 August (AOD ≈ 1), the resulting changes in SSA were approximately ±0.0002, ±0.005, and ±0.007 at 440, 380, and 340-325 nm, respectively. For the lower AOD cases on 27-28 August, SSA errors at these wavelengths were much smaller (<±0.0005). Increasing (decreasing) aerosol layer height is found to produce positive (negative) errors in SSA. Overall, the errors in the SSA induced by uncertain aerosol layer height are minor compared with those arising from individual uncertainties in the input AERONET AOD and MFRSR measurements. Furthermore, errors in the spectral SSA arising from the uncertain real part of the refractive index (RR) by ±0.05 are also quantified. We find that a negative (positive) change in RR by 0.05 results in negative (positive) errors in SSA of -0.008 at 440 nm and ~0.006 at UV wavelengths.

We also conducted a theoretical sensitivity analysis for quantifying the changes in the derived SSA at 440 nm due to different choices of dust aspect ratio distribution. The AERONET Level 1.5 direct AOD and inversion parameters, including PSD, real and imaginary parts of the refractive index, and surface albedo, were used to simulate the surface-level, synthetic diffuse-to-direct (DD) downwelling irradiance ratio (as it would have been measured by the MFRSR sensor). Three aspect ratio distributions were considered: 1) Dubovik et al. (2006) distribution, 2) OMI empirical distribution adopted in this work, and 3) spherical particles (i.e., aspect ratio=1.0). The synthetic DD ratios were used as measurements for the retrieval of SSA at 440 nm assuming three aspect ratio scenarios independently. The retrieval procedure and the software kept identical to the one used for inversion of actual MFRSR observations. For the comparison, SSA derived assuming Dubovik et al. (2006) aspect ratio distribution were treated as a reference.

Figure 9 demonstrates that the SSA derived assuming a) OMI empirical aspect ratio distribution and b) spherical particle assumption yield a consistent positive bias of 0.014 and 0.012, respectively, for measurements of AOD440>0.4, relative to those derived assuming spheroidal distribution proposed in Dubovik et al. (2006). These results, based upon the synthetic DD ratio simulation using actual AERONET inversion data, suggest noticeable sensitivity of the choice of dust aspect ratio distribution on the SSA retrievals from MFRSR ground sensor, where the

empirical distribution adopted in the present work as well as spherical dust model tested in the inversion procedure would result in higher SSA. Table 4 lists the uncertainties in the derived SSA attributed to each identified source of errors.

The sensitivity analysis presented above establishes the error characteristics in MFRSR-retrieved aerosol absorption parameters, where the uncertainty in the input AOD is a dominant factor in governing the resulting errors in the retrieved spectral *k* and SSA. The interpolated AOD values at 340, 380, and 440 nm are expected to be as reliable as the original AERONET AOD measurements. In contrast, the AOD values at 332 nm and 325 nm are extrapolated and may carry larger uncertainties than the nominal ±0.02. Consequently, errors in the retrievals of *k* and SSA may be higher than those reported above at these two shortest UV wavelengths. The total uncertainty in the retrieved aerosol absorption reflects the combined influence of all error sources discussed. In the real world, individual errors may partially cancel if they occur with opposite signs, or, in the worst case, compound to produce a larger total error.

5 RESULTS

5.1 SSA RETRIEVALS AT 440 NM AND ITS COMPARISON AGAINST AERONET

In Figure 10(a), we compare the MFRSR-derived SSAs at 440 nm against those of AERONET for a transported Saharan dust event observed between August 26-28, 2020. The SSAs are compared for the coincident AOD ranges $0.2<AOD_{440}<0.4$ (blue circles) and $AOD_{440}>0.4$ (red circles). Vertical gray bars represent 1-standard deviation of MFRSR SSAs retrievals at a 1-minute frequency collocated within ±30 minutes of the AERONET inversion. The resulting statistics of the comparison are included within the plot. The remaining three panels of Figure 10 (b, c, d) show the true-color satellite images, visually illustrating the dust transport, captured from the VIIRS sensor onboard Suomi-NPP satellite over the Tenerife Island for the respective days. We find that all matchup data points were contained within the ±0.03 error limits, which is the expected uncertainty in the AERONET SSA inversions at $AOD_{440}=0.4$. Sinyuk et al. (2020) have shown that the uncertainty in AERONET SSA decreases significantly for AOD_{440} greater than 0.4. Furthermore, the data points (in red) corresponding to higher aerosol loading conditions ($AOD_{440}>0.4$) showed a relatively lower SSA in the range ~0.91-0.95; lower AOD conditions (<0.4) result SSA in the range ~0.93-0.95. Figure 11 displays the intraday evolution of the spectral SSA derived from the MFRSR (colored circles) and the AERONET SSA at 440 nm (black circles). Each circle represents 30-minute averaged SSAs from the two respective sensors. Vertical lines show the expected uncertainty or total error in the MFRSR-derived SSAs calculated as $\sqrt{\varepsilon_{AOD}^2 + \varepsilon_{DD}^2}$.

Here, ε_{AOD} and ε_{DD} are the systematic uncertainties in SSA caused by uncertain AERONET AOD by ±0.01/±0.02 and random uncertainties due to 1% error in the measured diffuse-to-direct irradiance ratio, respectively. The 30-minute averaged AOD for each interval is printed next to the respective circles. The daily-averaged spectral AOD and SSA are printed below each plot. The Saharan dust transport over the Tenerife Island resulted in higher aerosol loading (AOD~1.0) on August 26, followed by relatively lower aerosol loading (AOD~0.5-0.4) on the following two days. Despite a significant reduction in the total aerosol loading above the Izaña site on August 26 and August 27, the

derived spectral SSA from the MFRSR shows a similar intraday pattern and magnitude, indicating the stability of the inversion at lower and higher aerosol loadings. The spectrally dependent SSA follows the behavior of the known dust aerosols exhibiting decreasing SSA at shorter wavelengths (Di Biagio et al., 2019). On all three days of dust transport, the SSA at all wavelengths (325 nm to 440 nm) from near noon to late evening, especially at shorter wavelengths, show an increasing trend. This is also indicative in the AERONET SSA inversions at 440 nm, albeit with a smaller increase relative to the shorter UV wavelengths.

The impact of the choice of the aspect ratio distribution of the spheroidal dust on the retrievals of SSA has also been examined. Figure 12 compares the MFRSR-derived *k* (a, b) and SSA (c, d) at 440 nm under two scenarios: 1) AERONET-like 'mixing" approach combining sphericity-weighted randomly oriented spheroids (Dubovik et al., 2006) and spheres and (2) employing an empirically derived distribution used in space-based aerosol retrievals over the ocean from near-UV sensors. In the first approach, the diffuse-to-direct irradiance ratios were simulated assuming spheroid and sphere separately and then linearly mixed by using the sphericity parameters of AERONET as follows:

$$DDRatio_{LUT} = DDRatio_{sphere} * Sph_{frac} + DDRatio_{spheroiod} * (1 - Sph_{frac})$$

Where, $DDRatio_{LUT}$ is the sphericity-weighted simulation of diffuse-to-direct (DD) ratio simulation (LUT), $DDRatio_{sphere}$ is the simulation for purely spherical particles, and $DDRatio_{spheroid}$ is the simulated DD ratio simulated using the Dubovik et al. (2006) aspect ratio, and Sph_{frac} is the AERONET-provided sphericity fraction. The $DDRatio_{LUT}$ as a function of the nodes in the imaginary part of the refractive index are then used to retrieve *k* and SSA.

When compared against AERONET inversion data, *k* (SSA) retrievals at 440 nm derived following the AERONET-like mixing approach show a positive (negative) bias of 0.0011 and 0.0005 (0.022 and -0.011) for AOD_{440} ranges of 0.2-0.4 and >0.4, respectively. In contrast, *k* (SSA) inversions made assuming the fixed, empirical distribution yield significantly lower biases of 0.0005 and -0.0001 (-0.014 and -0.002) for the respective AOD ranges. Root-mean-square-difference (RMSD) and number of SSA matchups falling within ±0.03 uncertainty limits also show noticeable improvement from 58% to 87% and 86% to 98% for the two AOD ranges, respectively. A limited comparison of the scattering phase function F11 for the three dust events displayed in Figure 5 showed close agreement in SSA between the two approaches. On the other hand, when applied to a much larger set of observations, the use of fixed, empirical aspect ratio provides improved comparison of MFRSR retrievals against AERONET.

Given the similar assumptions of PSD, real part of refractive index, AERONET-like spheroid and sphere mixing approach, and surface albedo, one would expect a close agreement between AERONET and MFRSR. Despite consistent assumptions, the MFRSR-derived SSAs are found to be biased lower by 0.02. Several factors, including dust shape factor, could have contributed to these observed discrepancies. Surface is assumed to be a Lambertian reflector against Ross–Li BRDF implemented in AERONET, which is not explicitly addressed in the present work. Other factors, such as iterative versus LUT-based retrieval approaches produced even smaller SSA differences, typically within 0.005. Moreover, the LUT nodes in the imaginary part of the refractive index are closely spaced,

reducing the effect of non-linearity in the inversion. Such changes in the original inversion code were primarily made for improving computational efficiency.

We adopted the empirically derived continuous dust aspect ratio distribution, shown as the "red curve" in Figure 5(a), in the present work because of two supporting reasons: 1) the location of the ground instrument on Tenerife Island is more representative of the over-ocean dust retrievals, for which the same distribution model used in the near-UV satellite aerosol retrievals showed improvements, and 2) resulting level of agreement between the MFRSR- and AERONET-derived SSA at 440 nm, as shown in Figure 12. However, we do not claim that this empirically derived aspect ratio distribution is applicable globally and, therefore, we don't intend to suggest replacing the distribution proposed in Dubovik et al. (2006).

A year-by-year comparison of the derived SSA at 440 nm between the two sensors is presented in Figure 13. A notable finding is the strong agreement observed in 2020 and 2021, with mean biases of -0.003 and 0.007 and RMSD of 0.013 and 0.011, respectively. In contrast, MFRSR SSA for 2022 and 2023 exhibits relatively larger positive biases of 0.021 and 0.010 and RMSD of 0.024 and 0.017, respectively, in cases with higher aerosol loading ($AOD_{440} > 0.4$). This interannual variability in the apparent bias suggests that the elevated SSA values in 2022 and 2023 may be linked to remaining calibration issues in the MFRSR retrievals. Specifically, the current calibration method for direct and diffuse irradiance is based upon relatively clean conditions ($AOD_{440} < 0.10$) and subsequently applied to days with higher aerosol loading ($AOD_{440} > 0.2$) on a monthly basis. Any changes in the instrument's performance during specific months between cleaner and aerosol-laden conditions, therefore, may introduce systematic errors in SSA retrievals.

5.2 Multi-year UV to VIS Spectral SSA Inversions

The observations recorded by MFRSR Head 582 at Izaña have been processed individually at all wavelengths to create a multi-year dataset of spectral aerosol absorption. Figure 14 displays the monthly times series of spectral SSAs, in the format of a box and whisker plot, at all five wavelengths of MFRSR. Grey boxes and whiskers represent the 25th-75th percentile range and 1.5 times the interquartile range, respectively; circles and horizonal lines are mean and median of the data for each month. Only the best SSA retrievals corresponding to the AERONET AOD>0.4 at the respective wavelengths and AERONET Extinction Ångström Exponent< 0.6 (440-870 nm) were included in the timeseries charts. SSA datasets at all five wavelengths, specifically at shorter UV wavelengths, show distinct interannual and intraseasonal variations. First, the SSA at UV wavelengths during the summer months of 2020 and 2023 are found to be lower in magnitudes (more aerosol absorption) as compared to those during the years 2021 and 2022. A large spread in the SSA data was also noticed in the month of July 2020. Second, a well-defined intraseasonal pattern in the SSA can be seen during the summer months, especially in 2021 and 2022, where SSA are found to be lowest in June and gradually increasing until October. An exception to this pattern is the month of August, where the spectral SSA at all wavelengths show a slight dip in the magnitude. Both the interannual and intraseasonal variations in spectral SSA are of prime interest for the estimation of dust radiative forcing, its influence on the atmospheric stability, and aerosol-cloud interactions. The interannual and intraseasonal variations in spectral SSAs, beyond the

range of their expected uncertainty of 0.02-0.03, are indicative of diverse sources of dust emissions having distinct absorption properties.

Figures 15, 16, and 17 summarize the combined spectral retrievals from 2019 to 2023 for the imaginary part of the refractive index, the single-scattering albedo, and the aerosol absorption optical depth respectively. The data are presented separately for the summer months of June through September as box and whisker plots, where orange and light-blue boxes represent retrievals from the MFRSR (440 nm to 325 nm) and AEROENT (440 nm to 1020 nm), respectively. Retrieval instances with AERONET-measured AOD>0.4 and Extinction Ångström Exponent (440-870 nm) <0.6 are included in the plots to restrict the analysis to moderate to higher dust aerosol loading, thus minimizing the uncertainty in the aerosol absorption inversion at lower AODs in both AERONET and MFRSR datasets. During the peak months of Saharan dust transport to the Atlantic Ocean and over the Izaña site (June through September), the imaginary part of the refractive index and AAOD both exhibit a weak spectral trend in the visible to near-IR region (AERONET) but a distinct increasing trend towards shorter UV wavelengths—a typical and expected spectral absorption behavior of coarse-mode dust aerosols (Kandler et al., 2007; Wagner et al., 2012). The SSA shows weak absorption with SSA values in the range 0.98-1.00 at red (675 nm) and longer wavelengths but decreases rapidly at 440 nm followed by a sharp decline at the UV wavelengths. The aerosol Absorption Ångström Exponent (AAE) values calculated for the MFRSR UV to visible light range (325-440 nm) are found to be noticeably larger than that calculated using the AERONET visible to near-IR dataset (440-870 nm).Seasonally, the AAE values are found to be largest in June (4.52), with a monotonic decrease as the season advances, reaching to the lowest value (2.02) in September. The intraseasonal variations in all three retrieved quantities show the largest absorption, but with significant variability in July and August, followed by relatively moderate absorption in June, and the lowest absorption strength (SSA>0.9) with minimal variability in September.

The spectral imaginary part of the complex refractive index retrieved from both MFRSR and AERONET observations is compared with laboratory-based *k* measurements of dust samples reported in the literature. Wagner et al. (2012) conducted a detailed retrieval analysis of five different Saharan dust aerosol samples representing diverse mineralogical compositions collected from locations such as Burkina Faso, Cairo, and during the SAMUM field campaign. Using an inversion scheme based on a spheroidal particle model, the study retrieved refractive indices over the 305–955 nm wavelength range. The retrieved *k* exhibited significant variability across the different samples, with *k* values ranging from approximately 0.005 to 0.02 at ~450 nm, and from ~0.01 to 0.03 at ~350 nm, with overall uncertainties in the range of 0.002 to 0.01. Another Izaña-specific study by Kandler et al. (2007) derived the chemical composition and complex refractive index of transported Saharan mineral dust during July and August 2005, based on a mineralogical model derived from electron microscopy. The study reported a *k* value of 0.009, which closely aligns with the *k* value of 0.007 at the same wavelength obtained from the direct optical measurements by Patterson et al. (1977).

Biagio et al (2019) conducted extensive in situ measurements of the imaginary part of the refractive index *k* and SSA over the spectral range 370-950 nm of mineral dust aerosol samples collected from 19 globally distributed dust sources, including the Saharan and Sahelian Deserts. Of particular interest to the present study, the Saharan Desert was

represented by soil samples collected from eight locations, where *k* values at 370 nm ranged from 0.0011 to 0.0088, with mean values of 0.0033 and 0.0049 for the North Africa-Saharan and Sahelian samples, respectively. The corresponding in-situ measurements of SSA at 370 nm for those soil samples were found in the range 0.85-0.92. The MFRSR-retrieved *k* values at 380 nm in the present study, on an average, range between 0.003 to 0.006, depending on the month of observations, with an upper bound value of ~0.009 observed in July. The corresponding monthly mean SSA values at 380 nm lie between 0.86-0.88 during June through August. While the averaged dust spectral absorption obtained in Biagio et al (2019) was consistent with that retrieved from AERONET-based inversion (Dubovik et al., 2002) and Balkanski et al. (2007) for dust with a 1.5% volume fraction of hematite content, the spectral *k* and SSA values across near-UV to near-IR wavelengths were systematically lower than those reported in several earlier in situ and satellite-based studies. Nonetheless, we find that the MFRSR-retrieved *k* and SSA values at the Izaña site align closely with the equivalent in-situ based measurements reported in Biagio et al. (2019) for the North African-Sahara and Sahel desert areas.

The spectral *k* values retrieved from the MFRSR and AERONET in the UV and visible ranges in this study (see Figure 15), and those obtained by Biagio et al. (2019), are significantly lower than those reported in previous studies discussed above. A key factor contributing to this discrepancy, beyond the inherent uncertainties in both in-situ and remote sensing techniques, may lie in the fundamental differences in measurement approaches. Laboratory measurements are typically performed on particles extracted from aerosol samples under controlled conditions, whereas ground-based and satellite remote sensing retrievals represent effective column-averaged aerosol properties in their ambient atmospheric conditions. Additionally, the dust aerosols observed at the Izaña site could be originated from different sources depending on wind directions and speed, potentially leading to observations that reflect either the optical characteristics of a dominant dust source or a mixture of multiple sources.

6 Conclusion and Final Remarks

We presented a multi-year, UV-VIS spectral aerosol absorption dataset collected at the Izaña Observatory, Tenerife Island, by the modified ground-based UV-Vis MFRSR instrument. The Izaña site offers a unique setting for ground-based atmospheric dust aerosol remote sensing for two main reasons: 1) its proximity to the Saharan desert enables sampling of transported dust plumes, and 2) its high elevation of ~2.4 km offers exceptionally cleaner atmospheric conditions on non-dusty days for accurate on-site calibration of the measurements. The MFRSR on-site calibration procedure used in this study, as described in section 2.2, differs from that employed in previous field deployments. Specifically, the partitioning of total spectral irradiance measured by the MFRSR into direct and diffuse components was adjusted, while keeping the total irradiance unchanged, based on space-time collocated AERONET spectral AOD during dusty conditions ($AOD_{440} > 0.2$). The modified calibration procedure applied to the MFRSR measurements uses monthly median value of calibration constant derived from observations on cleaner days. Furthermore, the aerosol absorption retrieval algorithm was updated from an iterative approach to a LUT-based method. This new method incorporates on-line RT simulations generated for 15 discrete values of the imaginary part of the refractive index. The LUT-based inversion significantly improves stability and resolves convergence issues noted in the earlier iteration-based approach.

A sensitivity analysis aimed to quantify the uncertainties in the retrieved *k* and SSA showed that the uncertainties in the AERONET spectral AOD (±0.01 at 440 nm ±0.02 at shorter UV wavelengths) represent the primary source of error, with resulting errors as large at ±0.06 at UV wavelengths for AOD<0.4. A 1% error in the MFRSR-measured diffuse-to-direct irradiance ratios and ± 1km uncertainties in the prescribed aerosol layer height in the LUT calculation produce significantly lower uncertainties compared to those produced by uncertain spectral AOD. Overall, the combined errors in the retrieved SSA at all five MFRSR wavelengths generally remain within ±0.03 for AOD larger than 0.4. The derived SSA at 440 nm exhibited sensitivity to the choice of dust aspect ratio distribution, demonstrating that the empirical distribution adopted in the present work as well as spherical dust model tested in the inversion procedure resulted in higher SSA compared to those retrieved from AERONET-like spheroids and sphere combination approach.

The SSA comparison at 440 nm, the common wavelength between AERONET and the MFRSR, showed close agreement, where almost all spacetime collocated matchup data were found to agree within ±0.03 uncertainty range of AERONET inversions at AOD_{440}>0.4. This agreement was a crucial step toward establishing a consistency between the two independent measurement and inversion techniques. We investigated the impact of two different approaches accounting for the particle aspect ratio distributions on SSA retrievals: (1) AERONET-like 'mixing" approach linearly combining sphericity-weighted randomly oriented spheroids (Dubovik et al., 2006) and spheres, and (2) an empirically derived distribution assumed in space-based near-UV aerosol retrieval algorithms. The latter is characterized by a continuous, smooth profile of aspect ratio representing spherical and spheroidal particles. Our findings showed that the AERONET-like approach of mixing spheroid and sphere distribution in the MFRSR inversion tends to underestimate SSA by -0.022 and -0.011 for lower ($0.2< AOD_{440} <0.4$) and higher ($AOD_{440} > 0.4$) aerosol loading conditions. In contrast, the empirically derived distribution resulted in significantly improved agreement with AERONET SSA at 440 nm, exhibiting relatively lower bias of -0.014 and -0.002, respectively. Based on these results, we adapted the empirically derived dust aspect ratios in all on-the-fly RT calculations used in the MFRSR inversion algorithm.

The multi-year UV-VIS spectral SSA time series reveal notable intra-seasonal and interannual variability. At shorter UV wavelengths, SSA generally exhibits a clear increasing trend from June through October—coinciding with the peak dust transport season—except for August, which consistently shows a deviation with lower SSA values. Interannually, SSA during the summer months increased from 2020 to 2022, followed by a noticeable decline in 2023. Another important finding is the significantly higher variability in MFRSR-derived SSA at UV wavelengths compared to the relatively stable and less-variant SSA retrieved by AERONET at visible-near Infrared (440-1020 nm) wavelengths. This pronounced variability in the UV spectral region suggests the presence of dust from diverse sources with different absorption characteristics as detected over the Izaña site, highlighting the distinct sensitivity of UV SSA to varying mineralogy of dust aerosols.

The multiyear UV-VIS spectral aerosol absorption information derived from the MFRSR observations at the Izaña Observatory site in Tenerife Island provides a unique and valuable dataset for studying optical properties of Saharan dust aerosols. The ground-based column aerosol SSA inversions at UV wavelengths is crucial for evaluating the concurrent space-based solar back-scatter UV (BUV) aerosol absorption retrievals, such as from AURA-OMI, DSCOVR-EPIC, PACE-OCI, and European BUV missions: S4, S5, S5p-TROPOMI. The availability of the ground-based columnar aerosol SSA inversion datasets eliminates the need to extrapolate satellite-based BUV aerosol SSA to AERONET's 440 nm retrievals, thereby reducing the associated uncertainties in the evaluation of satellite-ground BUV aerosol SSA comparison. Since July 2024, the re-calibrated UV-VIS MFRSR # 582 instrument has been redeployed alongside the sea-level AERONET site at Santa Cruz on Tenerife Island to evaluate BUV aerosol SSA retrievals from the Ocean Color Instrument (OCI) aboard NASA's PACE satellite. The Unified Aerosol Algorithm (UAA) applied to the OCI-measured UV to SWIR spectral observations utilizes the AOD derived from the combined Dark Target and Deep Blue algorithms in constraining the heritage near-UV aerosol algorithm to retrieve SSA and effective aerosol layer height (https://pace.oceansciences.org/data_table.htm).

The aerosol UV absorption data derived from the MFRSR sensor will be useful to estimate the direct radiative effects of mineral dust aerosols, the surface UV radiation, atmospheric stability, and tropospheric photochemistry. A key result from the MFRSR dust record at the Izaña site is the enhanced dust absorption of solar radiation at UV wavelengths, exhibiting significant temporal variability, much larger than at visible and NIR wavelengths. These variations are likely linked to changes in the mineralogical composition of dust aerosols. For instance, the iron-oxide content of atmospheric dust, although in smaller proportion compared to overall mass (~1%-3% by volume, Wagner et al., 2012), can have significant radiative impact in the shortwave spectral domain. Hematite and Goethite are key components of mineral dust determining the strength of light absorption due to their significantly larger (~100 times) imaginary part of the refractive index as compared to other soil mineral components. Among these two components, the imaginary index of hematite is significantly higher than that of goethite at the visible and UV wavelengths (Go et al., 2022, Figure 1). Such pronounced differences in their spectral absorption characteristics enable a clear separation between the two. Biagio et al (2019) also noted that the sample-to-sample variability in the measured *k* and SSA values of mineral dust samples collected over diverse dust sources were mostly linked linearly to the mass concentration of the iron oxide, hematite, and goethite, and total elemental iron content.

Go et al. (2022) demonstrated the potential of using BUV-visible observations from DSCOVR-EPIC to retrieve hematite and goethite volume fractions and mass concentrations in airborne dust over various arid regions. The spectral aerosol absorption data retrieved from the MFRSR offer similar opportunities of conducting such compositional inference analysis, which is encouraged as a direction for future research. The retrieval of spectral aerosol absorption properties and subsequent inference of the mineralogical composition of ambient dust aerosols will contribute to their accurate representation in Earth System Models, thereby enhancing our ability to quantify their climate impacts.

AUTHOR CONTRIBUTION

HT and NK conceptualized the study and performed the inversion procedure. JM and GL prepared the merged AERONET-MFRSR dataset, while NK updated the on-site MFRSR calibration procedure and HJ processed the data using the algorithm developed for deriving the inversion dataset presented in this paper. SK refactored and validated the original DLS reading/interpolating package. WG, GJ, SS, DS, KL, and CW, co-authors from Colorado State University and NOAA Central UV Calibration Facility (CUCF), conducted the maintenance and laboratory calibration of the MSFRSR instrument prior to its deployment at the Izaña site. AB and RG supervised and maintained the daily operations of the instrument at the Izaña Observatory. DF provided the radiative transfer model used for the LUT calculations. HJ led the manuscript writing, with all co-authors contributing to revisions and improvements. OT supervised the overall workflow, ensuring scientific integrity and accuracy.

CODE AND DATA AVAILABILITY

The code and results shown in the present paper can be obtained from the first authors upon request. The MFRSR inversion dataset presented in this paper will be made deposited in FAIR-aligned data repositories.

COMPETING INTERESTS

The lead author and at least one of the (co-)authors are members of the editorial board of Atmospheric Measurement Techniques.

ACKNOWLEDGMENTS

The authors are grateful to AERONET team and staff for their efforts in maintaining AERONET site at the Izaña site and made the direct sun and inversion products available to the community. The AERONET deployment is a part of the activities of the WMO-Measurement Lead Centre for aerosols and water vapor remote sensing instruments (MLC). The AERONET sun photometers at the Izaña Observatory (IZO) were calibrated through the AEROSPAIN Central Facility (https://aerospain.aemet.es/), supported by the European Community Research Infrastructure Action under the ACTRIS grant (agreement no. 871115).

APPENDIX:

Summary of Changes in Light Single Scattering Simulation (DLS package)

The Appendix summarizes our simplifications implemented in the original DLS reader/interpolator (Dubovik et al., 2006) that improved the MFRSR algorithm's computational performance. In what follows, DLS refers to the original package; our reader/interpolator is referred to as the API (Application Programming Interface).

DLS (Dubovik et al., 2006) is a FORTRAN code that calculates radiative parameters (extinction and absorption coefficients, and the phase matrix) for light scattered once by randomly oriented spheroids, based on their optical (real n and imaginary k parts of the refractive index) and geometric (radius r of an equivalent volume sphere, in μm, and aspect ratio ε distributions, $D(r)$ and $D(\varepsilon)$, respectively) parameters, and the particle column concentration.

To expedite these calculations, DLS uses two types of the look-up tables (LUTs), also called kernels. First are "main" kernels **K** of size ~5 GB defined on the specific grids of all the mentioned parameters. The fixed kernels **k** are precomputed from the main **K**-s for a given aspect ratio distribution $D(\varepsilon)$. The LUT approach accelerates the calculation of the radiative parameters from the fixed kernels **k** using, as input, a user-defined (bimodal) size distribution function, particle column concentration, and wavelength λ. DLS defines the kernels **K** and **k** for a fixed λ = 0.340μm because the mentioned radiative parameters depend on the size parameter $x = 2\pi r/\lambda$.

However, the implementation of reader/interpolator in DLS was found to be time-consuming for our purpose given the 1-minute intervals of a multi-year MFRSR observational record. Both **K** and **k** are stored in ASCII (text) format, with arrays of different sizes and shapes located in the same file. For instance, the phase matrix as a function of scattering angle is provided for subsequent calculations, while the r-grid is stored just for reference. The MFRSR retrieval algorithm calls either DLS or the API iteratively as a precompiled executable. This simplifies switching between the two packages but requires re-reading of **k** at each iteration, since memory is released after each call. It is therefore crucial for us to store the fixed kernels in a format that can be read efficiently.

On top of that, DLS interpolates the fixed kernels **k** over the size r to a user-defined r-grid prior to averaging over it. Before switching to the API, the MFRSR algorithm used the following r-grids (floating-point numbers are truncated for convenience). For **k**, the r-grid spans 0.0033μm to 25.82μm, equidistantly spaced on a logarithmic scale with

$\Delta\ln(r) = 0.1180$, total 34 grid nodes. The user r-grid spans 0.05μm to 15.0μm with the same constant $\Delta\ln(r)$, total 22 grid nodes. Due to the similarity of the two grids, and despite the extra 12 r-grid points, it is faster to integrate over the **k**'s r-grid directly, without interpolation to the user r-grid. Instead of the lognormal size distribution $D(\ln(r))$, we use the size parameter distribution $D(\ln(x))$ for integration over particle size. The latter is a matter of convenience, not performance.

To create the API, numerically equivalent to the original DLS reader/interpolator yet optimized for our needs, we did the following:

1. For a fixed aspect ratio distribution $D(\varepsilon)$, we generated the fixed kernels **k** using the original DLS package, whose "main" kernels **K** are described in (Dubovik et al., 2006). DLS prints **k** in the text format along with auxiliary parameters such as grids of scattering angles and particle size.
2. To speed up iterative reading of the fixed kernels **k** in our algorithm, we converted the **k** files from text to binary format. The auxiliary parameters are now hardcoded in the API. As a result, the API reads **k** with a single C-language command (see next step). However, the user must be mindful of endianness (the order in which bytes are stored: https://en.wikipedia.org/wiki/Endianness). We provide the **k**-converter code as open source (see the second-to-last paragraph of this Appendix). In addition to the conversion, the **k**-converter reads back the binary data and compares it with the original DLS text files.
3. A few subroutines of the original DLS FORTRAN code responsible for reading and interpolating the fixed kernels **k** were manually translated into C/C++. This work was initiated as part of the translation of MAIAC's (Lyapustin et al., 2021) polarized radiative transfer solver IPOL (Korkin and Lyapustin, 2023) from FORTRAN into C. Note, however, that it is not the change of language that contributes to speeding up, but the changes described in the previous and next steps.
4. Interpolations over the size r and the scattering angle were dropped from the API as unnecessary for our workflow. To get the size-averaged radiative parameters, we also integrate in the $\ln(x)$ space using the same x-grid as in the fixed kernel **k**. The same applies to the scattering angle: the API calculates the phase matrix on the fixed kernels grid, from 0° to 180° in steps of 1°.
5. The DLS code contains two parts: calculation **k** from **K**, and calculation of radiative properties from **k**. Our refactoring was applied only to the part utilizing the fixed kernels **k** because it is called iteratively in the MFRSR retrieval algorithm. Hence, its high efficiency is crucial. We have not changed the part of DLS that calculates **k** from **K**; nor have we altered the "main" LUTs **K**.

In summary, our API performs three steps: (*a*) reads the fixed kernels **k** from seven binary files (six for the elements of the phase matrix and one for the combined scattering and extinction coefficients); (*b*) performs bilinear interpolation over the real and imaginary parts of the refractive index for the user-provided values; (*c*) integrates over the size parameter x.

The API has been validated in multiple ways. First, it was tested against DLS, both acting as stand-alone codes, to confirm they produce the same output (extinction, single scattering albedo, and all elements of the phase matrix) for

the same input. The typical relative difference was a tiny fraction of percent, except at exact forward scattering, due to integration over r up to 25μm (**k** grid default upper limit) rather than 15μm (user grid default upper limit).

Next, the MAIAC LUTs used for polarization correction of MODIS, VIIRS, DSCOVR/EPIC, and S5P/TROPOMI data (i.e., different bands and scattering geometries) over land and ocean (i.e., different aerosol models) were reproduced using the API and compared with those previously generated using DLS. The averaged difference in TOA reflectance was ~0.5% and, since 2023, MAIAC has used the API to generate LUTs for polarization correction.

Before implementing the API into the MFRSR retrieval algorithm, we performed an additional numerical test with the OMI empirical aspect ratio distribution $D(\varepsilon)$ shown in Fig. 5(a) (note: MAIAC uses that from AERONET). We found relative differences in the extinction and single scattering albedo to be 0.1% and 0.2%, respectively. For all elements of the phase matrix, the deviation oscillates within ±0.5%, reaching its highest values at the forward (0^o) and back (180^o) scattering angles. At, e.g., 90^o scattering angle and for the averaged scattering cosine, the deviations were 0.05% and 0.03%, respectively.

We ran the MFRSR retrieval algorithm, first with DLS and then with the API, which can be switched easily in our application. We found the influence of the above-mentioned differences on the retrieval outcome to be insignificant. For example, the SSA result at 0.440μm was found to be 0.005 units lower for the API as compared to DLS, which is within our retrieval uncertainty. In contrast, the reduction in the MFRSR algorithm's execution time was so obvious that we deemed exact quantification of the speed-up unnecessary. We further extended the performance testing of the API against original DLS software package on a larger synthetic downwelling surface diffuse-to-direct ratio dataset simulated using the actual AERONET Lev 1.5 direct and inversion datasets for 2020 at the Izaña site. These dust measurements were treated as spherical particles in both inversion runs. The resulting SSA retrievals at 440 nm showed negligible differences between the two software tools with root-mean-square-difference and mean bias in SSA remained very low (0.002-0.003). The level of agreement found in these comparisons demonstrated consistency between two tools, ruling out any major errors or biases in simulating phase matrices with modified API tool.

We presented the API at the AERONET Science and Application Exchange (Korkin et al., 2024a) and at an AGU session dedicated to AERONET's 30th Anniversary (Korkin et al., 2024b). The API is available at https://github.com/korkins/spheroids with documentation. The code for converting the fixed kernels to binary format is in the same GitHub repository, under /convert_kernels_src_linux/, with step-by-step instructions and a reproducible example.

In conclusion, we reiterate that our improvements are relevant only to the reading/interpolating part (the API) of the original DLS package (Dubovik et al., 2006); we added nothing to the scientific kernels **K** described therein. The GRASP Team (https://www.grasp-open.com/) has improved the original DLS package: https://code.grasp-open.com/open/spheroid-package/. However, we have not evaluated their new implementation because the original stable version of the DLS package was sufficient for our specific needs.

REFERENCES

Ahn, C., Torres, O., Jethva, H., Tiruchirapalli, R., & Huang, L.-K.: Evaluation of aerosol properties observed by DSCOVR/EPIC instrument from the Earth-Sun Lagrange 1 Orbit. Journal of Geophysical Research: Atmospheres, 126, e2020JD033651, doi: https://doi.org/10.1029/2020JD033651, 2021.

Aryasree, S., Kandler, K., Benker, N., Walser, A., Tipka, A., Dollner, M., Seibert, P., and Weinzierl, B.: Vertical Variability in morphology, chemistry and optical properties of the transported Saharan air layer measured from Cape Verde and the Caribbean, Royal Society Open Science, 11(11), doi: https://doi.org/10.1098/rsos.231433, 2024.

Balkanski, Y., Schulz, M., Claquin, T., and Guibert, S.: Reevaluation of Mineral aerosol radiative forcings suggests a better agreement with satellite and AERONET data, Atmos. Chem. Phys., 7, 81-95, doi: https://doi.org/10.5194/acp-7-81-2007, 2007.

Barreto, Á., García, R. D., Guirado-Fuentes, C., Cuevas, E., Almansa, A. F., Milford, C., Toledano, C., Expósito, F. J., Díaz, J. P., and León-Luis, S. F.: Aerosol characterisation in the subtropical eastern North Atlantic region using long-term AERONET measurements, Atmos. Chem. Phys., 22, 11105-11124, https://doi.org/10.5194/acp-22-11105-2022, 2022.

Bohren, C. F. and Singham, S. B.: Backscattering by nonspherical particles: A review of methods and suggested new approaches, J. Geophys. Res., 96(D3), 5269-5281, doi: https://doi.org/10.1029/90JD01138, 1991.

Campanelli, M., Estellés, V., Colwell, S., Shanklin, J., and Ningombam S. S.: Analysis of aerosol optical properties from continuous sun-sky radiometer measurements at Halley and Rothera, Antarctica over seven years, Geophysical Research Abstracts, Vol. 17, EGU2015-2768, EGU General Assembly, Vienna, Austria, 12–17 April 2015.

Caudill, T.R., Flittner, D.E., Herman, B.M., Torres, O., McPeters, R.D.: Evaluation of the pseudo-spherical approximation for backscattered ultraviolet radiances and ozone retrieval, J. Geophys. Res., 102(D3), 3881-3890, https://doi.org/10.1029/96JD03266, 1997.

Corr, C. A., Krotkov, N., Madronich, S., Slusser, J. R., Holben, B., Gao, W., Flynn, J., Lefer, B., and Kreidenweis, S. M.: Retrieval of aerosol single scattering albedo at ultraviolet wavelengths at the T1 site during MILAGRO, Atmos. Chem. Phys., 9, 5813–5827, https://doi.org/10.5194/acp-9-5813-2009, 2009.

Di Biagio, C., Formenti, P., Balkanski, Y., Caponi, L., Cazaunau, M., Pangui, E., Journet, E., Nowak, S., Andreae, M. O., Kandler, K., Saeed, T., Piketh, S., Seibert, D., Williams, E., and Doussin, J.-F.: Complex refractive indices and single-scattering albedo of global dust aerosols in the shortwave spectrum and relationship to size and iron content, Atmos. Chem. Phys., 19, 15503–15531, doi: https://doi.org/10.5194/acp-19-15503-2019, 2019.

Dubovik, O., Holben, B. N., Eck, T. F., Smirnov, A., Kaufman, Y. J., King, M. D., Tanre, D., and Slutsker, I.: Variability of absorption and optical properties of key aerosol types observed worldwide locations, J. Atmos. Sci., 59(3), 590-608, doi: https://doi.org/10.1175/1520-0469(2002)059<0590:VOAAOP>2.0.CO;2, 2002.

Dubovik, O., Sinyuk, A., Lapyonok, T., Holben, B. N., Mishcenko, M., Yang, P., Eck, T. F., Volten, H., Munoz, O., Vehelmann, B., van der Zande, W. J., Leon, J. F., Sorokin, M., and Slutsker, I.: Application of spheroid models to account for aerosol particle nonsphericity in remote sensing of desert dust, J. Geophys. Res., 111, D11208, https://doi.org/10.1029/2005JD006619, 2006.

Eck, T. F., Holben, B. N., Reid, J. S., Dubovik, O., Smirnov, A., O'Neill, N. T., Slutsker, I., and Kinne, S.: Wavelength dependence of the optical depth of biomass burning, urban, and desert dust aerosols, J. Geophys. Res., 104(D24), 31333-31349, doi: https://doi.org/10.1029/1999JD900923, 1999.

Forster, P. M., et al. (2021). Chapter 6: Short-lived climate forcers. In V. Masson-Delmotte et al. (Eds.), Climate Change 2021: The Physical Science Basis. Contribution of Working Group I to the Sixth Assessment Report of the Intergovernmental Panel on Climate Change (pp. 817–922). Cambridge University Press. https://www.ipcc.ch/report/ar6/wg1/chapter/chapter-6/.

García, M. I., Rodríguez, S., and Alastuey, A.: Impact of North America on the aerosol composition in the North Atlantic free troposphere, Atmos. Chem. Phys., 17, 7387-7404, https://doi.org/10.5194/acp-17-7387-2017, 2017.

Go, S., Lyapustin, A., Schuster, G. L., Choi, M., Ginoux, P., Chin, M., Kalashnikova, O., Dubovik, O., Kim, J., da Silva, A., Holben, B., and Reid, J. S.: Inferring iron-oxide species content in atmospheric mineral dust from DSCOVR EPIC observations, Atmos. Chem. Phys., 22, 1395–1423, https://doi.org/10.5194/acp-22-1395-2022, 2022.

Harrison, L., Michalsky, J., and Berndt, J.: Automated multifilter rotating shadow-band radiometer: an instrument for optical depth and radiation measurements, Appl. Opt. 33 (22), 5118-5125, doi: https://doi.org/10.1364/AO.33.005118, 1994.

Harrison, L. and Michalsky, J.: Objective algorithms for the retrieval of optical depths from ground-based measurements, Appl. Optics, 33, 5126-5132, doi: https://doi.org/10.1364/AO.33.005126, 1994.

Hashimoto, M., Nakajima, T., Dubovik, O., Campanelli, M., Che, H., Khatri, P., Takamura, T., and Pandithurai, G.: Development of a new data-processing method for SKYNET sky radiometer observations, Atmos. Meas. Tech., 5, 2723–2737, https://doi.org/10.5194/amt-5-2723-2012, 2012.

Herman, B. M. and Browning, S. R.: A numerical solution to the equation of radiative transfer, J. Atmos. Sci., 22, 559-566, doi: https://doi.org/10.1175/1520-0469(1965)022<0559:ANSTTE>2.0.CO;2, 1965.

Intergovernmental Panel on Climate Change (IPCC). (2021). Climate Change 2021: The Physical Science Basis. Contribution of Working Group I to the Sixth Assessment Report of the Intergovernmental Panel on Climate Change. Cambridge University Press. https://www.ipcc.ch/report/ar6/wg1/.

Huang, Y., Kok, J. F., Kandler, K., Lindqvist, H., Nousiainen, T., Sakai, T., Adebiyi, A., Jokinen, O.: Climate models and remote sensing retrievals neglect substantial desert dust asphericity. Geophysical Research Letters, 47, e2019GL086592, doi: https://doi.org/10.1029/2019GL086592, 2020.

Kandler, K., Benker, N., Bundke, U., Cuevas, E., Ebert, M., Knippertz, P., Rodriguez, S., Schutz, L., and Weinbruch, S.: Chemical composition and complex refractive index of Saharan Mineral Dust at Izaña, Tenerife (Spain) derived by electron microscopy, Atmos. Environ., 41, 8058-8074, doi: https://doi.org/10.1016/j.atmosenv.2007.06.047, 2007.

Krotkov, N., Bhartia, P. K., Herman, J., Slusser, J., Labow, G., Scott, G., Janson, G., Eck, T. F., and Holben, B.: Aerosol ultraviolet absorption experiment (2002 to 2004), part 1: ultraviolet multi- filter rotating shadowband radiometer calibration and intercomparison with CIMEL sunphotometers, Opt. Eng., 44, 041001, doi: https://doi.org/10.1117/1.1886818, 2005a.

Krotkov, N., Bhartia, P. K., Herman, J., Slusser, J., Scott, G., Labow, G., Vasilkov, A. P., Eck, T. F., Dubovik, O., and Holben, B. N.: Aerosol ultraviolet absorption experiment (2002 to 2004), part 2: absorption optical thickness, refractive index, and single scattering albedo, Opt. Eng., 44, 041005, doi: https://doi.org/10.1117/1.1886819, 2005b.

Korkin, S., and Lyapustin, A.: Radiative interaction of atmosphere and surface: Write-up with elements of code, Journal of Quantitative Spectroscopy and Radiative Transfer, vol. 309: 108663, https://doi.org/10.1016/j.jqsrt.2023.108663, 2023.

Korkin, S., Lyapustin, A., and Holben, B.: AERONET Project: The Next 30 Years of Software Development, AERONET Science and Application Exchange, University of Maryland College Park MD, September 17-19, 2024(a) Link to poster: https://aeronet.gsfc.nasa.gov/new_web/AERONET_Exchange/2024/Posters/ASAE__SKorkin_ALyapustin_BHolben_Poster.pdf (accessed 2026/03/23)

Korkin, S., Lyapustin, A., Siniuk, A., Slutsker, I., Lind, E., and Holben, B.: AERONET Scientific Software After 30 Years: Time to Re-Optimize? American Geophysical Union Fall Meeting, Washington DC, USA, December 9-13, , Abstract #A11Q-1890, 2024(b)
Link to abstract: https://agu.confex.com/agu/agu24/meetingapp.cgi/Paper/1577853 (accessed 2026/03/23)

Lyapustin A., Go, S., Korkin, S., Wang, Y., Torres, O., Jethva, H., and Marshak, A.: Retrievals of Aerosol Optical Depth and Spectral Absorption from DSCOVR EPIC. Front. Remote Sens. 2:645794, doi: https://doi.org/10.3389/frsen.2021.645794, 2021.

Michalsky, J. J., Schlemmer, J. A., Berkheiser, W. E., Berndt, J. L., Harrison, L. C., Laulainen, N. S., Larson, N. R., and Barnard, J. C.: Multiyear measurements of aerosol optical depth in the Atmospheric Radiation Measurement and Quantitative Links programs. Journal of Geophysical Research, 106(D11), 12099-12107. doi: 10.1029/2001JD900096, 2001.

Mishchenko, M. I. and Travis, L. D.: T-matrix computations of light scattering by large spheroidal particles, Opt. Commun., 109, 16-21, doi: https://doi.org/ https://doi.org/10.1016/0030-4018(94)90731-5, 1994.

Mishchenko, M. I., Travis, L. D., Kahn, R. A., and West, R. A.: Modeling phase functions for dustlike tropospheric aerosols using a shape mixture of randomly oriented poly- disperse spheroids, J. Geophys. Res., 102, 16831-16847, https://doi.org/10.1029/96JD02110, 1997.

Mok, J., Krotkov, N., Arola, A., Torres, O., Jethva, H., Adrade, M., Labow, G., Eck. T., Li, Z., Dickerson, R., Stenchikov, G., Osipov, S., Ren, X.: Impacts of brown carbon from biomass burning on surface UV and ozone photochemistry in the Amazon Basin, Sci. Rep., 6, 36940, doi: https://doi.org/10.1038/srep36940, 2016.

Mok, J., Krotkov, N. A., Torres, O., Jethva, H., Li, Z., Kim, J., Koo, J.-H., Go, S., Irie, H., Labow, G., Eck, T. F., Holben, B. N., Herman, J., Loughman, R. P., Spinei, E., Lee, S. S., Khatri, P., and Campanelli, M.: Comparisons of spectral aerosol single scattering albedo in Seoul, South Korea, Atmos. Meas. Tech., 11, 2295–2311, https://doi.org/10.5194/amt-11-2295-2018, 2018.

Nakajima, T., Tonna, G., Rao, R., Boi, P., Kaufman, Y., and Holben, B.: Use of sky brightness measurements from ground for remote sensing of particulate polydispersions, Appl. Optics, 35, 15, 2672-2686, doi: https://doi.org/10.1364/AO.35.002672, 1996.

Panta, A., Kandler, K., Alastuey, A., González-Flórez, C., González-Romero, A., Klose, M., Querol, X., Reche, C., Yus-Díez, J., and Pérez García-Pando, C.: Insights into the single-particle composition, size, mixing state, and aspect ratio of freshly emitted mineral dust from field measurements in the Moroccan Sahara using electron microscopy, Atmos. Chem. Phys., 23, 3861–3885, https://doi.org/10.5194/acp-23-3861-2023, 2023.

Patterson, E. M., Gillette, D. A., and Stockton, B. H.: Complex index of refraction between 300 and 700 nm for Saharan aerosols, J. Geophys. Res., 82(21), 3153-3160, doi: https://doi.org/10.1029/JC082i021p03153, 1977.

Reid, E. A., Reid, J. S., Meier, M. M., Dunlap, M. R., Cliff, S. S., Broumas, A., Perry, K., and Maring, H.: Characterization of African dust transported to Puerto Rico by individual particle and size segregated bulk analysis, J. Geophys. Res., 108, 8591, D19, doi: https://doi.org/10.1029/2002JD002935, 2003.

Sinyuk, A., Holben, B. N., Eck, T. F., Giles, D. M., Slutsker, I., Korkin, S., Schafer, J. S., Smirnov, A., Sorokin, M., and Lyapustin, A.: The AERONET Version 3 aerosol retrieval algorithm, associated uncertainties and comparisons to Version 2, Atmos. Meas. Tech., 13, 3375-3411, https://doi.org/10.5194/amt-13-3375-2020, 2020.

Torres, O., Bhartia, P. K., Jethva, H., and Ahn, C.: Impact of the ozone monitoring instrument row anomaly on the long-term record of aerosol products, Atmos. Meas. Tech., 11, 2701–2715, https://doi.org/10.5194/amt-11-2701-2018, 2018.

Torres, O., Jethva, H., Ahn, C., Jaross, G., and Loyola, D. G.: TROPOMI aerosol products: evaluation and observations of synoptic-scale carbonaceous aerosol plumes during 2018–2020, Atmos. Meas. Tech., 13, 6789–6806, https://doi.org/10.5194/amt-13-6789-2020, 2020.

Yang, P. and Liou, K. N.: Geometric-optics-integral-equation method for light scattering by nonspherical ice crystals, Appl. Opt., 35, 6568-6584, doi: https://doi.org/10.1364/AO.35.006568, 1996.

Yang, P., Liou, K. N., Mishchenko, M. I., and Gao, B. C.: Efficient finite-difference time-domain scheme for light scattering by dielectric particles: Application to aerosols, Appl. Opt., 39, 3727-3737, doi: https://doi.org/10.1364/AO.39.003727, 2000.

Wagner, R., Ajtai, T., Kandler, K., Lieke, K., Linke, C., Müller, T., Schnaiter, M., and Vragel, M.: Complex refractive indices of Saharan dust samples at visible and near UV wavelengths: a laboratory study, Atmos. Chem. Phys., 12, 2491–2512, https://doi.org/10.5194/acp-12-2491-2012, 2012.

Waterman, P. C.: Symmetry, unitarity, and geometry in electromagnetic scattering, Phys. Rev., 825-839, doi: https://doi.org/10.1103/PhysRevD.3.825, 1971.

Table 1 MFRSR-AERONET, satellite sensors, and their respective datasets used in the present study.

Platform/ Instrument	Operation Period	Measurement Characteristics
MFRSR Instrument # 582	July 2019 - January 2024	Total and Diffuse Irradiance at 305, 311, 325, 332, 340, 380, 440 nm Temporal frequency: 1 minute
AERONET	July 2019 – January 2024 Contemporary to MFRSR	Direct Measurements: Version 3 Level 1.5 Spectral AODs at 325, 332, 340, 380, and 440 nm Extrapolated AODs at 325 and 332 nm Inversion Dataset: Version 3 Level 1.5 Particle size distribution, Real part of the refractive index at 440 nm.
Aura/OMI	July 2019 - January 2024	Total column O_3 and NO_2 amounts
SNPP/OMPS	July - September 2023	Total column O_3 amount
Pandora	July - September 2023	Total column O_3 and NO_2 amounts

1045

Table 2 MFRSR data availability at Izaña observatory at different wavelengths and corresponding valid numbers of aerosol absorption inversions. The multiplying factors for each MFRSR wavelength to create nodes in the imaginary part of the refractive index are listed at the end of the table.

Wavelength [nm]	**2019-08**		**2020**		**2021**		**2022**		**2023**	
	N_{meas}	N_{Inv}	N_{meas}	N_{Inv}	N_{meas}	N_{Inv}	N_{meas}	N_{Inv}	N_{meas}	N_{Inv}
440	1531	764 (50%)	10849	8297 (76%)	13245	7853 (59%)	9431	5968 (63%)	9192	5460 (59%)
380	1707	1119 (66%)	11019	9525 (86%)	14182	10856 (77%)	9586	8317 (87%)	9904	7939 (80%)
340	1739	1306 (75%)	11102	9741 (88%)	14623	11578 (79%)	9878	8826 (89%)	10193	8313 (82%)
332	1740	1322 (76%)	11111	9759 (88%)	14643	11646 (80%)	9912	8851 (89%)	10244	8425 (82%)
325	1741	1275 (73%)	1117	9704 (87%)	14663	11558 (79%)	9932	8827 (89%)	10285	8494 (83%)

N_{meas} = Total number of MFRSR measurements with AOD>0.2 and SZA<70°
N_{Inv} = Total number of valid inversions (% success rate)

Nodes in the imaginary part of the refractive index:
$N = IMGINDX440_{AERONET}$ * Multiplying Factors

Multiplying Factors:
440 nm: 0.4, 0.6, 0.8, 1.0, 1.2, 1.4, 1.6, 1.8, 2.0, 3.0, 4.0, 5.0, 6.0, 7.0, 8.0
380 nm: 0.5, 1.5, 2.5, 3.5, 4.5, 5.5, 6.5, 7.5, 8.5, 9.5, 10.5, 12.5, 14.5, 16.5, 18.5
340 nm: 0.5, 1.5, 2.5, 3.5, 4.5, 5.5, 6.5, 7.5, 8.5, 10.5, 12.5, 14.5 ,16.5, 20.5, 24.5
332 nm: 0.5, 1.5, 2.5, 3.5, 4.5, 5.5, 6.5, 7.5, 8.5, 10.5, 12.5, 14.5 ,16.5, 20.5, 24.5
325 nm: 0.5, 1.5, 2.5, 3.5, 4.5, 5.5, 6.5, 7.5, 8.5, 10.5, 12.5, 16.5, 20.5, 24.5, 28.5

Table 3 The weighting factor distributions of dust aspect ratios as a function of radius for randomly oriented spheroids proposed in Dubovik et al. (2006) and empirically derived factors employed in space-based near-UV aerosol retrievals as well as used in the present work.

Radius [μm]	**Dust Aspect Ratio Distribution**	
	Dubovik et al. (2006)	**Empirical (used in this work, red curve in Figure 5a)**
0.33490	0.0661850	0.0000000
0.36690	0.0650250	0.0000000
0.40190	0.0636350	0.0344414
0.44030	0.0620500	0.0365618
0.48230	0.0587200	0.0389464
0.52830	0.0533500	0.0416091
0.57870	0.0477625	0.0445430
0.63390	0.0429530	0.0477057
0.69440	0.0403205	0.0510056
0.76070	0.0000000	0.0542747
0.83330	0.0000000	0.0572537
0.91290	0.0000000	0.0596070
1.00000	0.0000000	0.0609579
1.09540	0.0000000	0.0610000
1.20000	0.0000000	0.0596000
1.31450	0.0000000	0.0568799
1.44000	0.0403205	0.0531880
1.57740	0.0429530	0.0490006
1.72800	0.0477625	0.0447783
1.89290	0.0533500	0.0408951
2.07360	0.0587200	0.0376011
2.27150	0.0620500	0.0350568
2.48832	0.0636350	0.0333685
2.72580	0.0650250	0.0000000
2.98600	0.0661850	0.0000000

1055

Table 4 Estimated uncertainties in the MFRSR-derived spectral SSA attributed to different sources of errors: ±0.01-0.02 error in the AERONET AOD, ±1% error in the MFRSR-measured diffuse-to-direct (DD) ratio, ±1 km change in aerosol layer height (ALH), ±0.05 change in assumed real part of the refractive index (RR), and change in dust aspect ratio distribution. Uncertainties in SSA due to errors in AOD and DD ratio represent averaged values derived from a large sampling dataset for different ranges in AOD observed during 2019-2023 MFRSR observation record, whereas those due to errors in ALH and RR were derived using a limited set of measurements acquired during August 26-28, 2020 (see Figure 10).

	ΔSSA due to change in spectral AOD (ΔAOD=±0.01 at 440 nm ΔAOD=±0.02 at UV Wavelengths)					
Wavelength	**AOD Range**					
	0.2-0.4	**0.4-0.6**	**0.6-0.8**	**0.8-1.0**	**1.0-1.2**	**1.2-1.4**
440 nm	0.031	0.019	0.013	0.009	0.008	0.007
380 nm	0.058	0.034	0.024	0.017	0.014	0.012
340 nm	0.053	0.031	0.023	0.016	0.013	0.013
332 nm	0.052	0.030	0.023	0.015	0.012	0.013
325 nm	0.050	0.030	0.022	0.015	0.012	0.013
	ΔSSA due to 1% change in MFRSR-measured diffuse-to-direct ratio					
440 nm	0.009	0.008	0.006	0.006	0.006	0.004
380 nm	0.011	0.008	0.007	0.006	0.006	0.004
340 nm	0.012	0.009	0.007	0.006	0.006	0.004
332 nm	0.012	0.009	0.007	0.006	0.006	0.004
325 nm	0.013	0.009	0.007	0.006	0.006	0.007
	ΔSSA due to change in dust aspect ratio distribution (Synthetic DD ratio analysis 2020)					
440 nm	**0.011**	**0.014**	**0.016**	**0.018**	**0.014**	**0.015**
	ΔSSA due to change in dust aspect ratio distribution (Actual MFRSR DD Ratio measurements 2020)					
440 nm	**0.011**	**0.017**	**0.024**	**0.024**	**0.038**	**0.015**

	ΔSSA due to change in ALH by ±1 km		**ΔSSA due to ±0.05 change in Real Part of Refractive Index (ΔRR)**	
	AOD~1.0	**AOD~0.4**	ΔRR=**-0.05**	ΔRR=**+0.05**
440 nm	0.002	0.0002-0.005	-0.0080	+0.0079
380 nm	0.005	0.001-0.002	-0.0066	+0.0066
340-325 nm	0.007	0.002-0.003	-0.0054	+0.0055

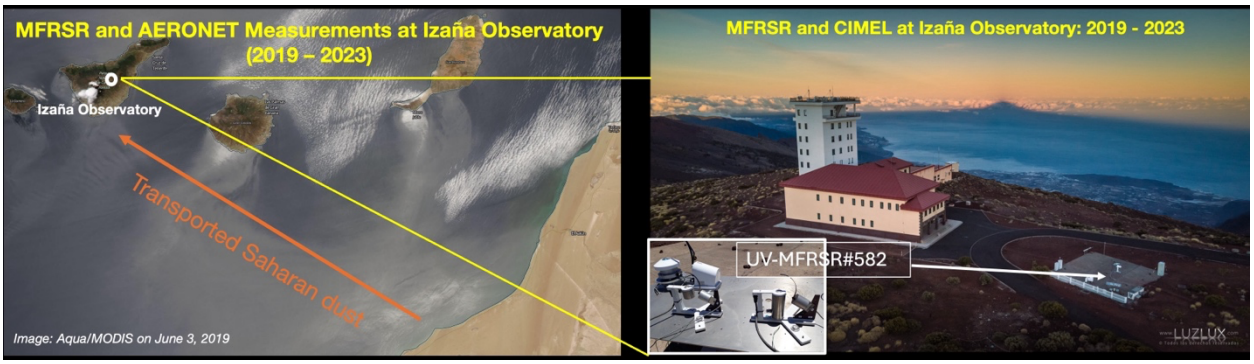

Figure 1. (Left) A synoptic view of the northwestern Sahara, Tenerife Island, and the location of the Izaña observatory seen in the Aqua/MODIS true-color RGB image acquired on June 3, 2019. (Right) An aerial photograph showing the installation of MFRSR instrument # 582 and AERONET CIMEL sun photometer at the Izaña observatory.

1070

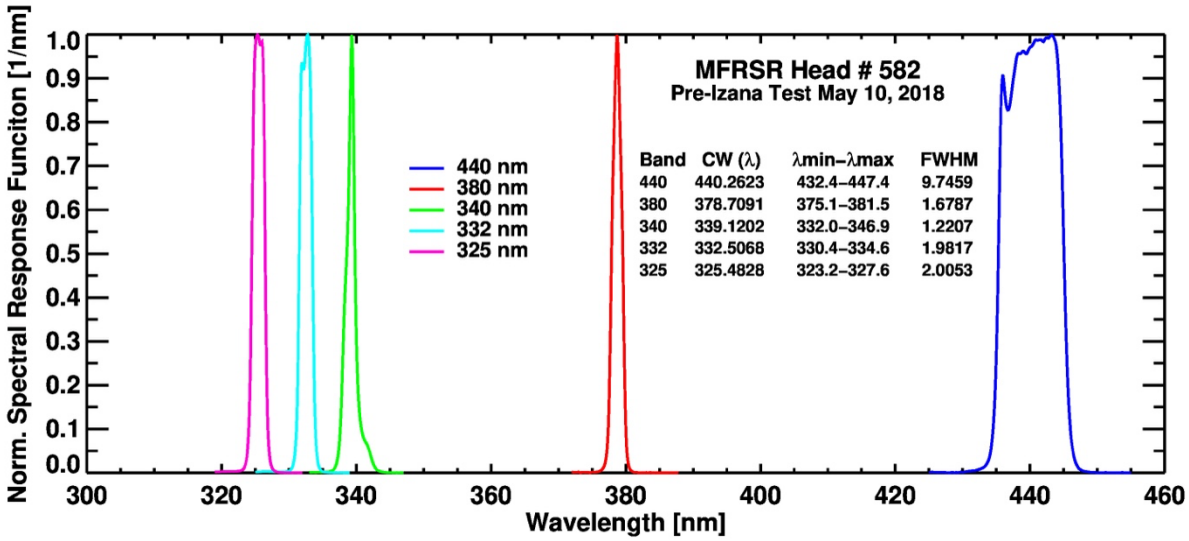

Figure 2. Normalized spectral response functions of the MFRSR head # 582 wavelength bands calculated prior to its deployment at the Izaña Observatory. Central Wavelength (CW), wavelength range (λ_{min}-λ_{max}), and full-half-maximum-width (FWHM) values for each band are printed within the plot.

1075

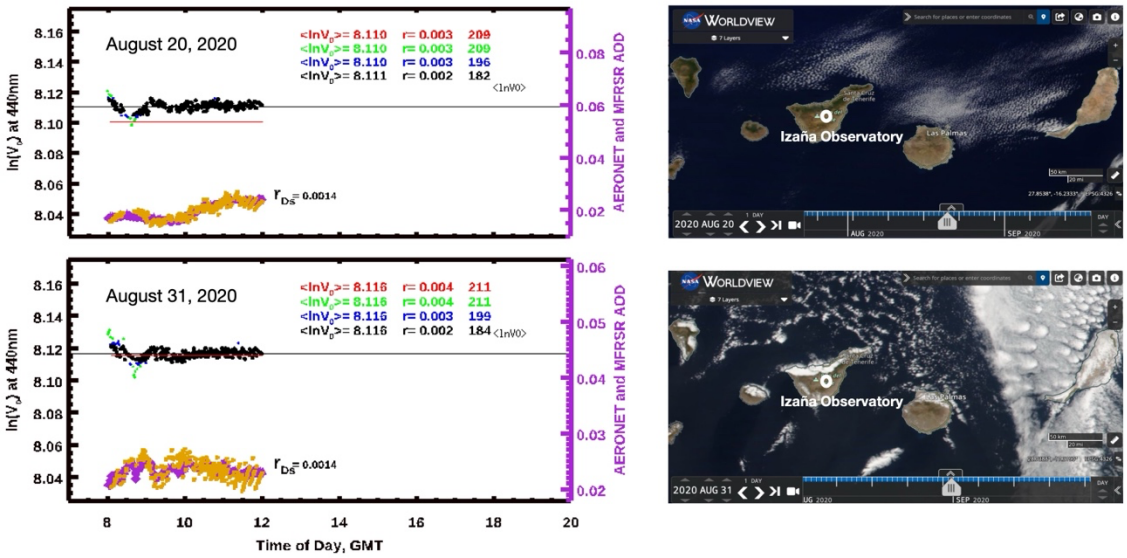

Figure 3. (Left) Examples of MFRSR Step 1 calibration plots on the cleaner days of August 20 and 31 of 2020, when AERONET-measured AODs (440 nm) were quite lower (<0.03). The logarithm of V_0 is shown against the left-hand y-axis as red-green-blue-black dots. The different colors show the effect of the iterative removal of V_0 outliers outside of 3σ standard deviation. The measured AODs from AERONET and the MFRSR instruments are shown as purple and orange dots, respectively, against the righthand y-axis. (Right) The MODIS true-color RGB images for the corresponding days showing a virtually aerosol-free atmosphere.

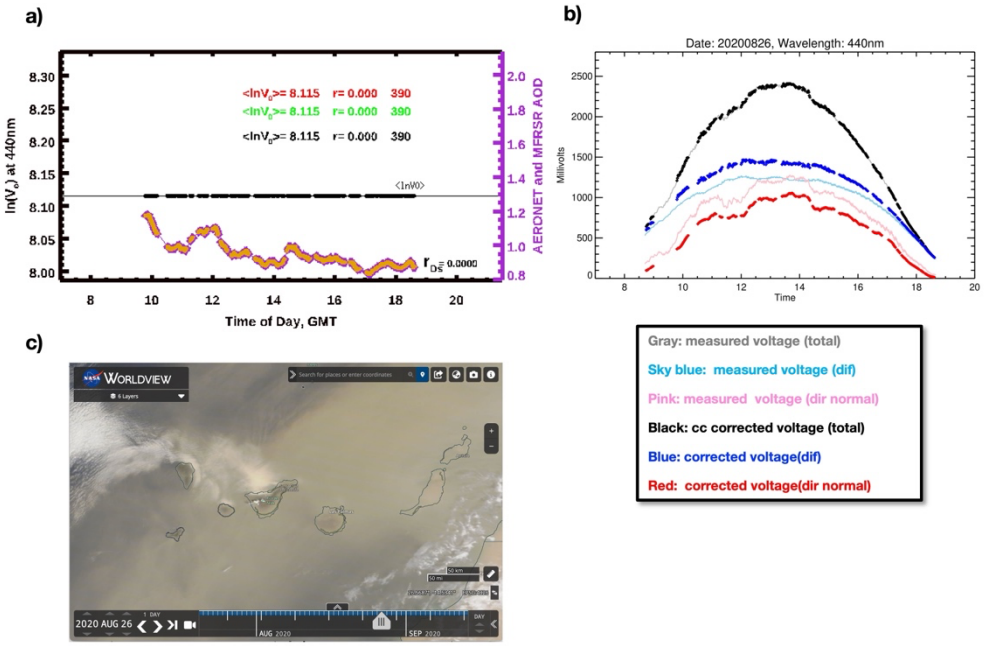

1085

Figure 4. An example of a) step-2 and b) step-3 of the calibration procedure for a dusty day of August 26, 2020. a) A constant value of ln(V_0) calculated from the step-1 is applied to the entire day of observations to calculate the corrected direct-normal voltage, shown as dark-blue dots on (b). The AERONET and MFRSR measured AODs are shown in orange and purple, respectively, on the right-hand side y-axis The corrected diffuse voltage (red curve), shown in (b),
1090 is calculated by subtracting corrected direct horizontal voltage from the cosine-corrected measured total voltage. c) the true-color RGB image acquired on the same day from Aqua-MODIS, showing the transport of massive dust plume over the observation site in Tenerife Island and adjacent Atlantic Ocean.

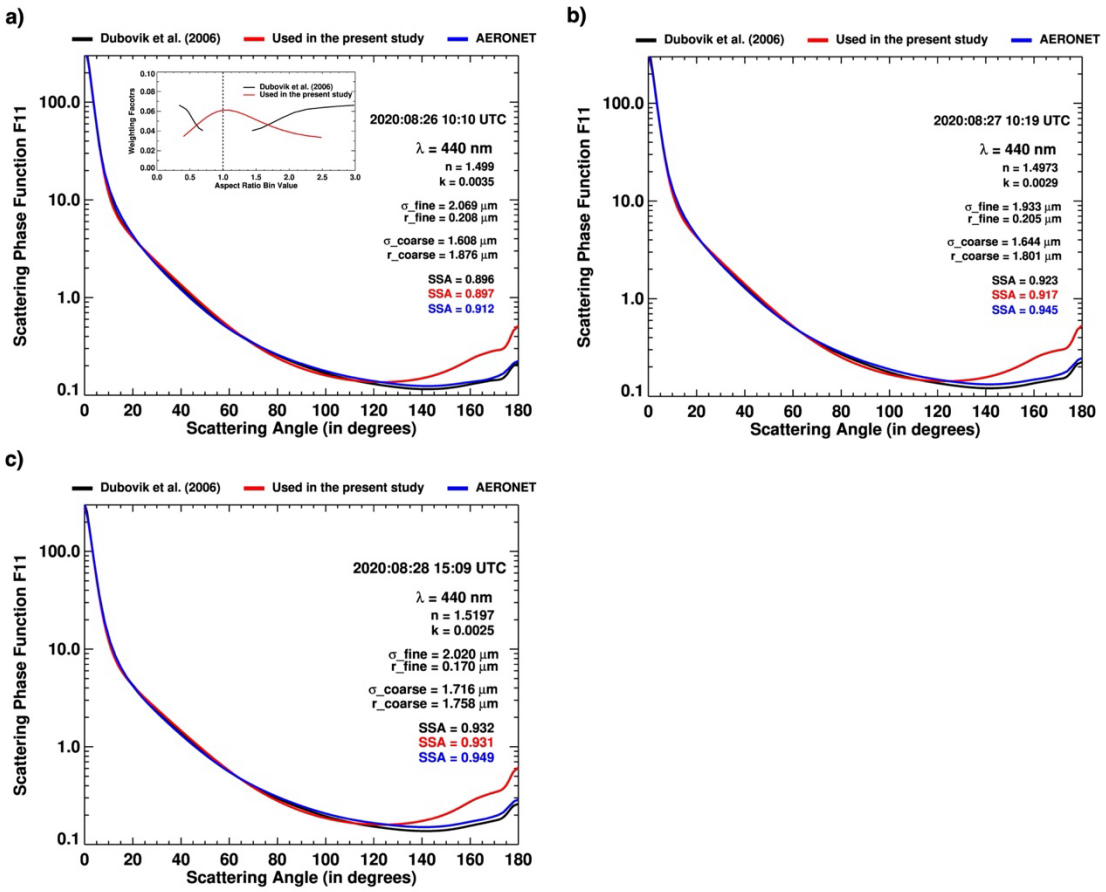

Figure 5. Scattering phase function F11 (440 nm) of mineral dust aerosols retrieved on a) August 26 at 10:10 UTC, b) August 27 at 10:19 UTC, and c) August 28 at 15:09 UTC of 2020 corresponding to randomly oriented spheroids proposed in Dubovik et al. (2006) (black), empirically derived distribution (red) used in the present study, and that from AERONET inversion product (blue). F11 (except for AERONET) was simulated using the modified DLS software package for a single MFRSR-AERONET collocated measurement for the respective dates. Dust aspect ratio distribution (black curves, Dubovik et al., 2006) and OMI empirical aspect ratio distribution used in the presented study (red curve) are shown as an inset in the top-left plot (a).

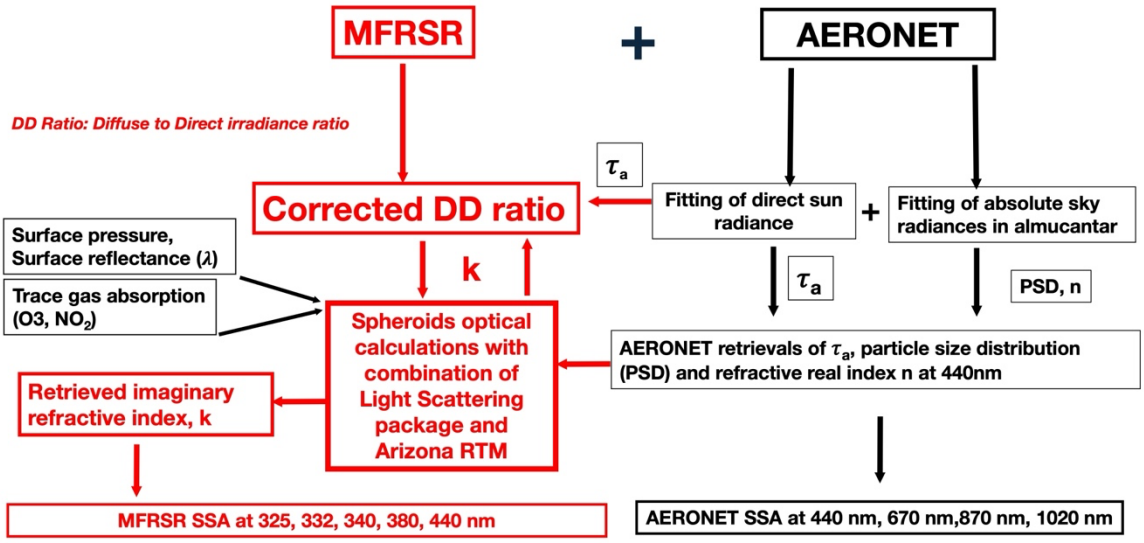

Figure 6. A simplified flowchart of the MFRSR-AERONET synergistic algorithm for the inversion of the UV-VIS spectral imaginary part of the refractive index and SSA.

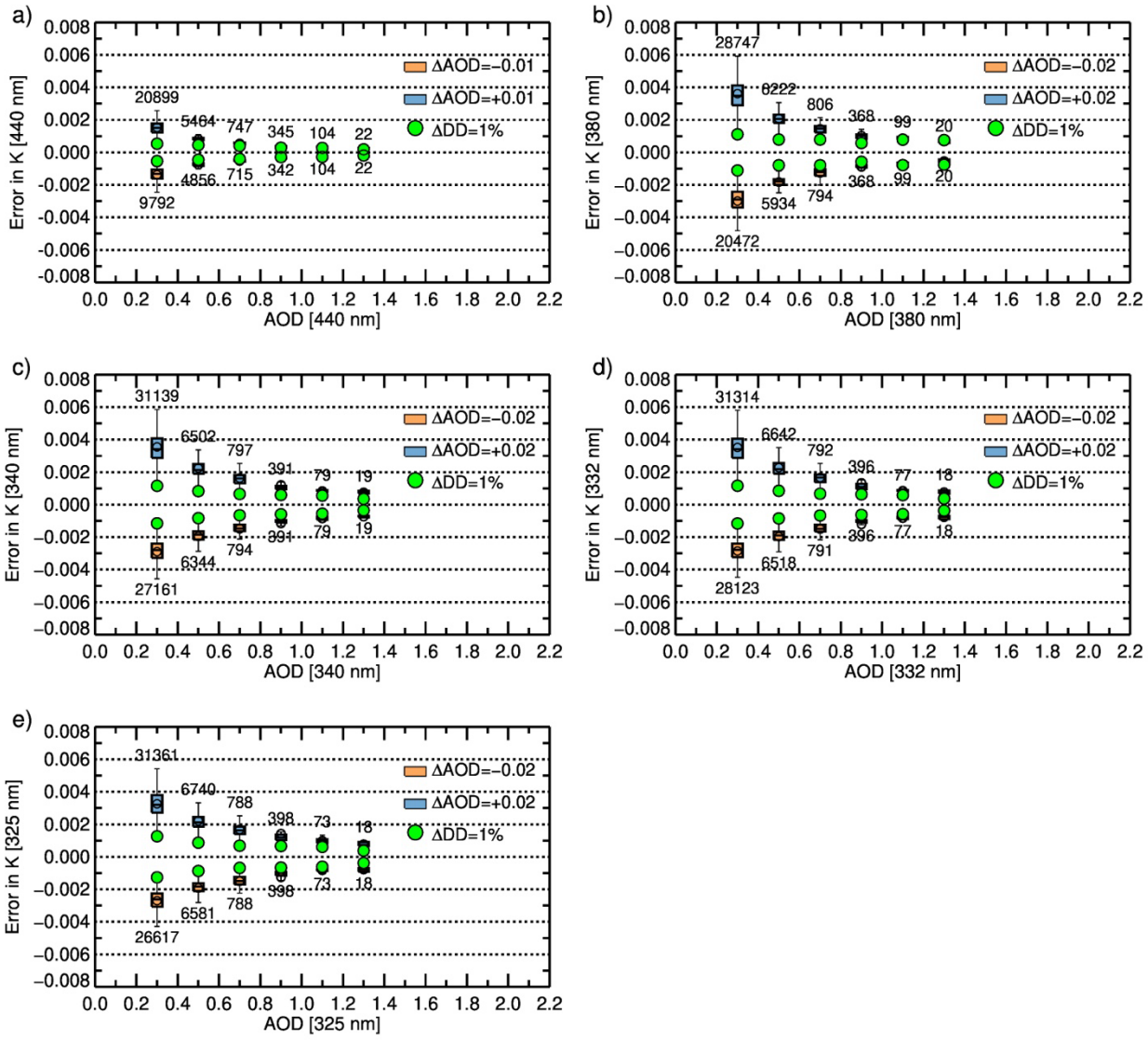

Figure 7. Errors in the MFRSR-retrieved spectral imaginary part of the index (*k*) resulting from 1) the uncertainties in the AERONET-measured AOD (orange and blue boxes) and 2) 1% change in the MFRSR-measured diffuse-to-direct irradiance ratio (filled green circles). Data represent MFRSR record from 2019-2023. Box-and-whisker elements indicate the interquartile range (25^{th}-75^{th} percentiles; boxes) and 1.5 times IQR (whiskers); mean values are shown as open circles and median values as horizontal lines.

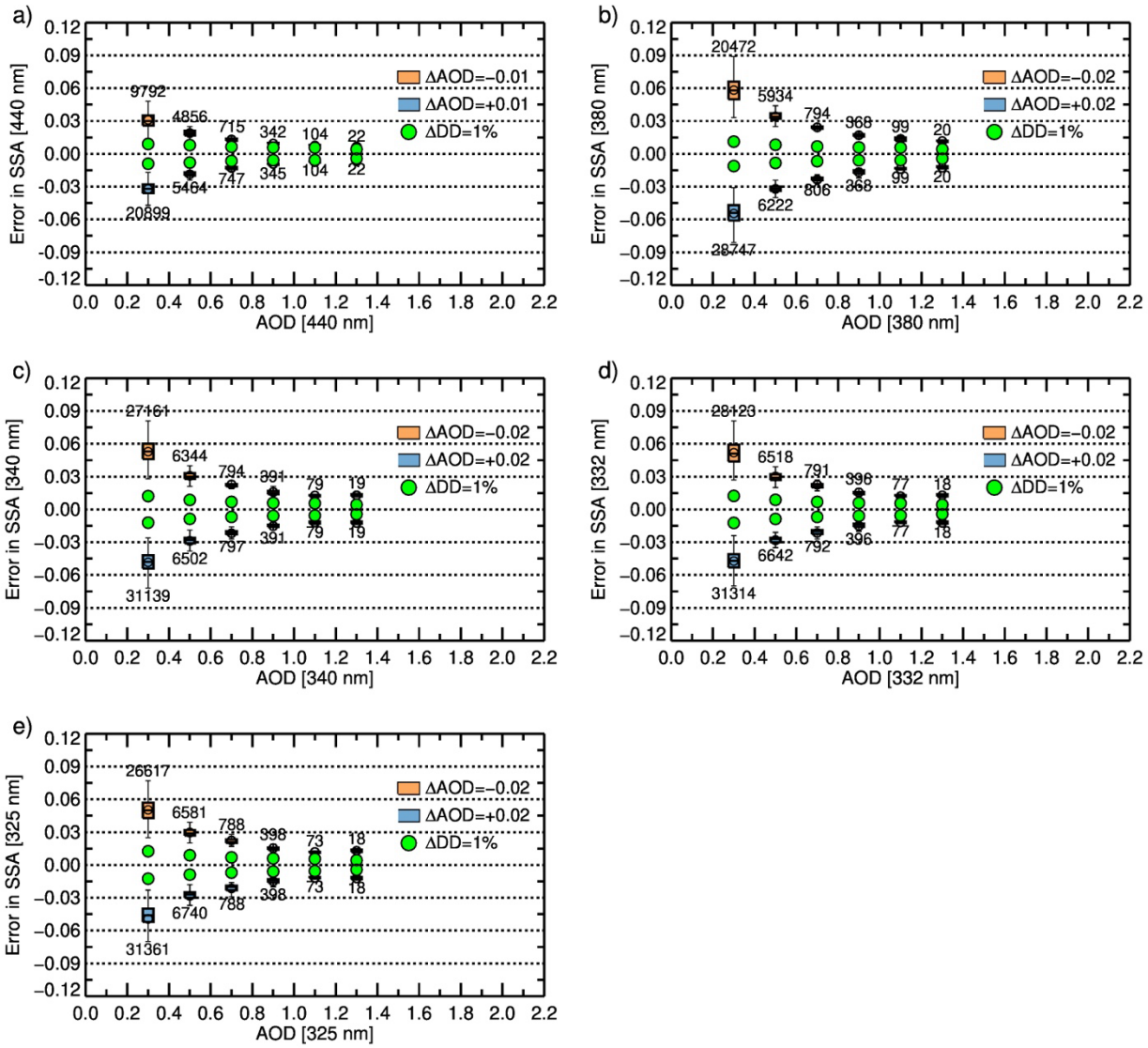

1115 **Figure 8.** Same as in Figure 7 but for the MFRSR-derived spectral SSA.

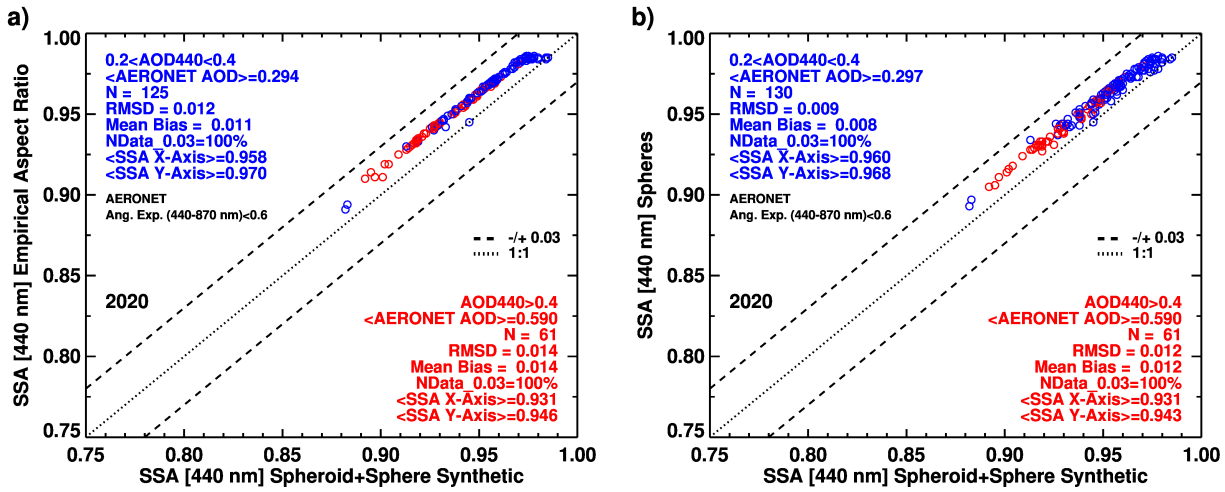

Figure 9 Comparison charts of SSA (440 nm) derived assuming a) empirical aspect ratio and b) spherical particles against those retrieved assuming AERONET-like spheroid-sphere combined approach. The synthetic diffuse-to-direct downwelling irradiance ratio simulated using actual AERONET Lev 1.5 inversion dataset collected at the Izaña site were treated as measurements in the inversion process. SSA matchup data points in blue and red represent the coincident AOD440 conditions of 0.2-0.4 and >0.4, respectively. The statistics of the comparison for different AOD conditions are included within the plots.

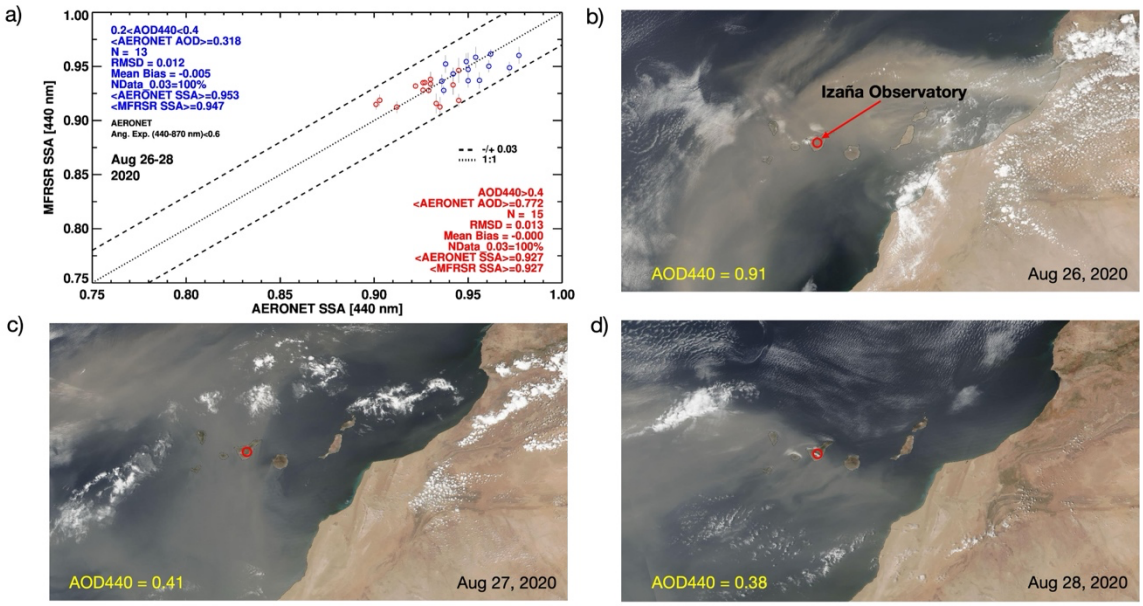

Figure 10. a) Comparison of the MFRSR vs. AERONET derived SSA at 440 nm for the data acquired on August 26, 27, and 28 of 2020. Blue and red circles represent temporally matched data with coincident AERONET-measured AOD (440 nm) 0.2-0.4 and >0.4, respectively. The statistics of the comparison for different AOD conditions are included within the plots. The true-color RGB images acquired from Suomi-NPP/VIIRS sensor for three dates are shown in b), c), and d).

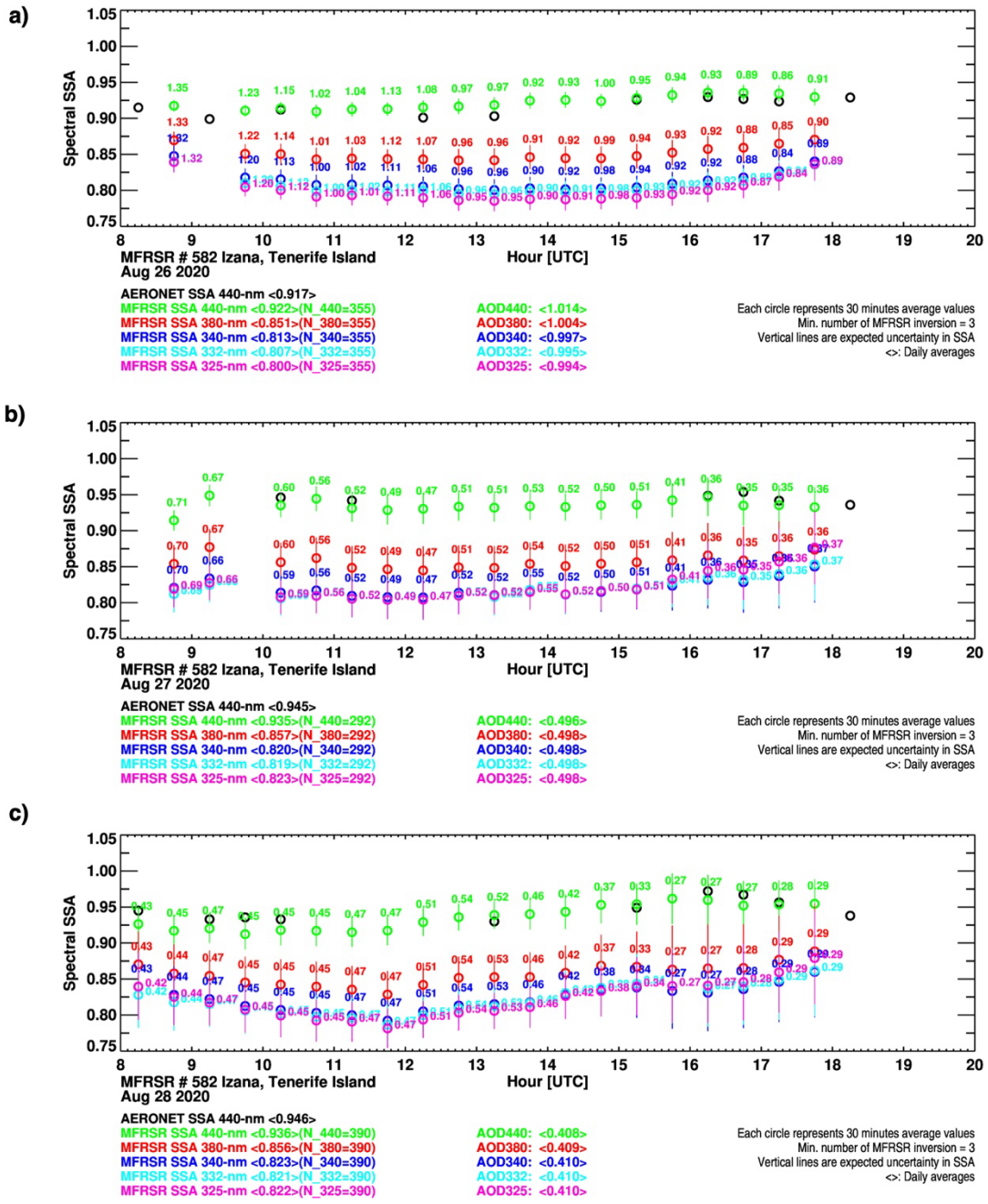

Figure 11. Sub-hourly spectral SSA derived from UV-VIS MFRSR observations acquired on August 26, 27, and 28 (a, b, c, respectively) of 2020. Each circle represents 30-minute averaged SSA values with corresponding averaged AOD printed next to it. Vertical lines represent the expected uncertainty in the derived SSA, which combinedly accounts for both ±0.01-0.02 uncertainties in the AERONET-measured AOD and a 1% error in the diffuse to direct irradiance ratio. Daily mean values of SSAs and AODs are printed on the bottom of each plot.

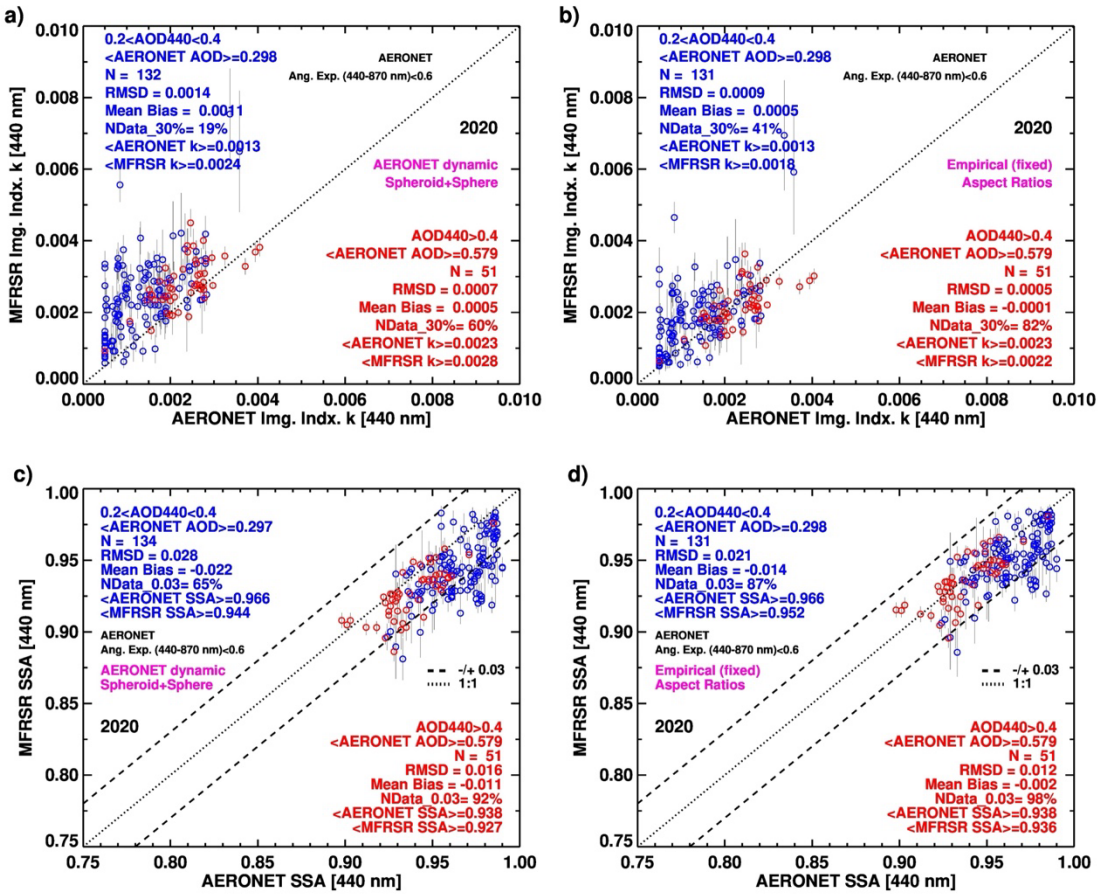

Figure 12. Comparison of MFRSR (y-axis) vs. AERONET (x-axis) collocated imaginary part of the refractive index (a, b) *k* and SSA (c, d) at 440 nm for the matchup data collected during 2020 at Izaña site derived assuming AERONET-like 'mixing" approach (a, c) combining sphericity-weighted randomly oriented spheroid (Dubovik et al., 2006) and sphere, and empirically derived aspect ratios (b, d) adopted in the over-ocean dust aerosol models used for near-UV aerosol algorithm of OMI, EPIC, and TROPOMI sensors. SSA matchup data points in blue and red represent the coincident AOD_{440} conditions of 0.2-0.4 and >0.4, respectively. The statistics of the comparison for different AOD conditions are included within the plots.

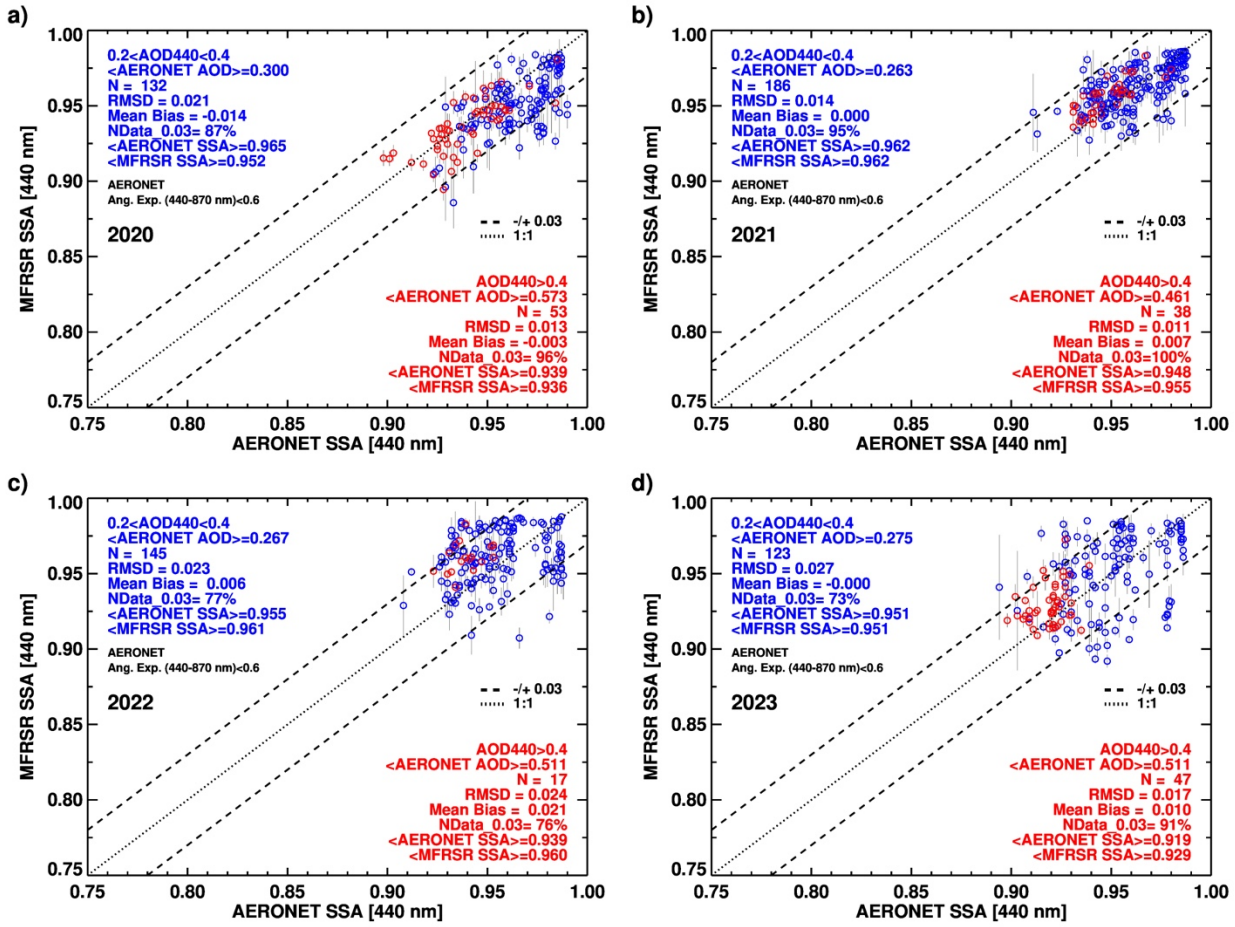

Figure 13. Comparison of MFRSR (y-axis) vs. AERONET (x-axis) SSA at 440 nm for the 2020-2023 (a though d) operation period of MFRSR measurements at Izaña site derived assuming empirically derived aspect ratios. Matchup data points in red (blue) represent AOD_{440}>0.4 (0.2<AOD_{440}<0.4) conditions. The statistical measures of the comparison are included within individual plot.

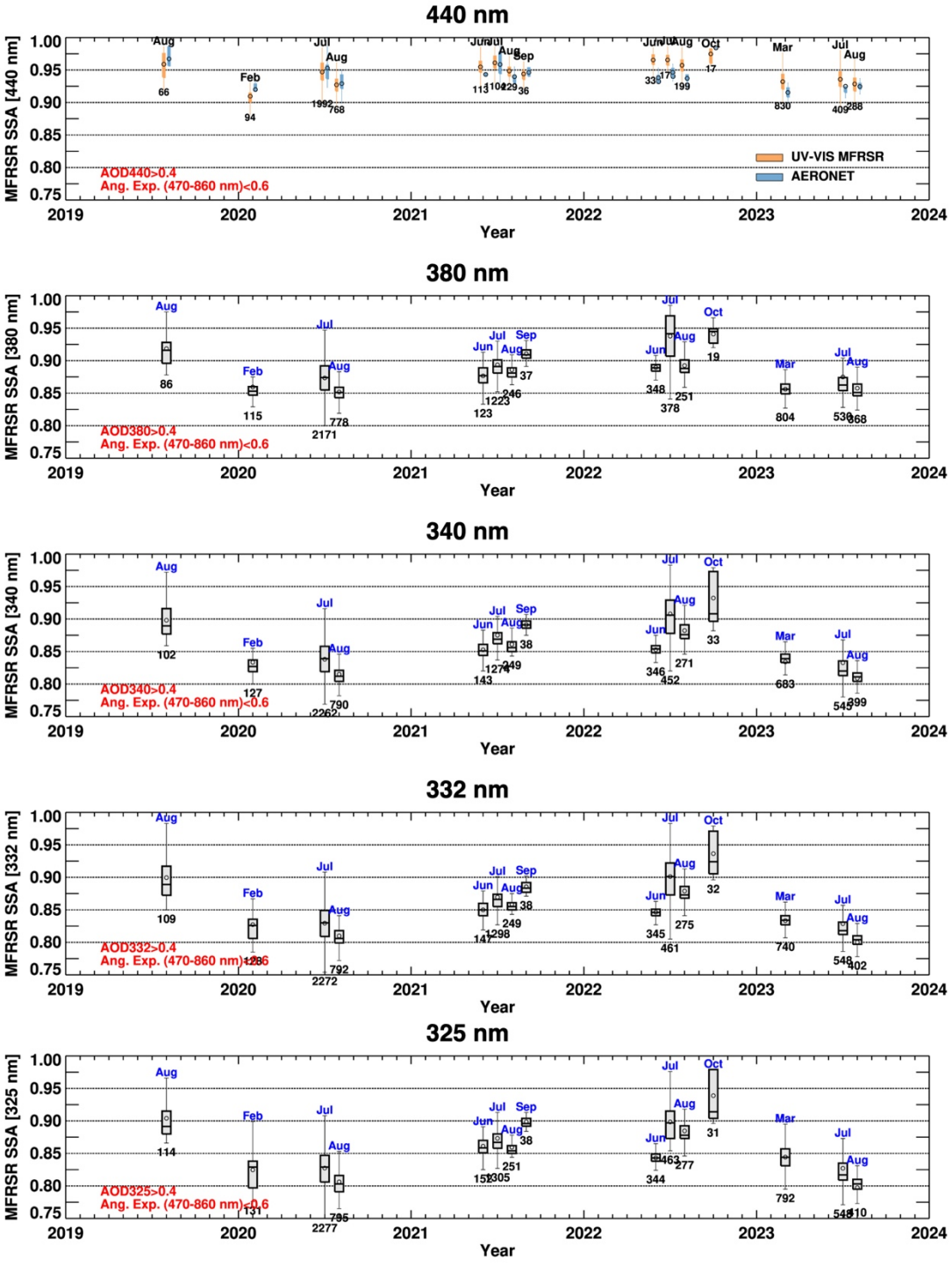

1155 **Figure 14.** Monthly time-series charts of MFRSR-derived spectral SSAs. The data are represented as box and whisker plot; grey boxes and whiskers represent 25th – 75th percentile range and 1.5 times the interquartile range, respectively. Data with AERONET AOD at respective wavelengths>0.4 and Extinction Ångström Exponent< 0.6 are presented.

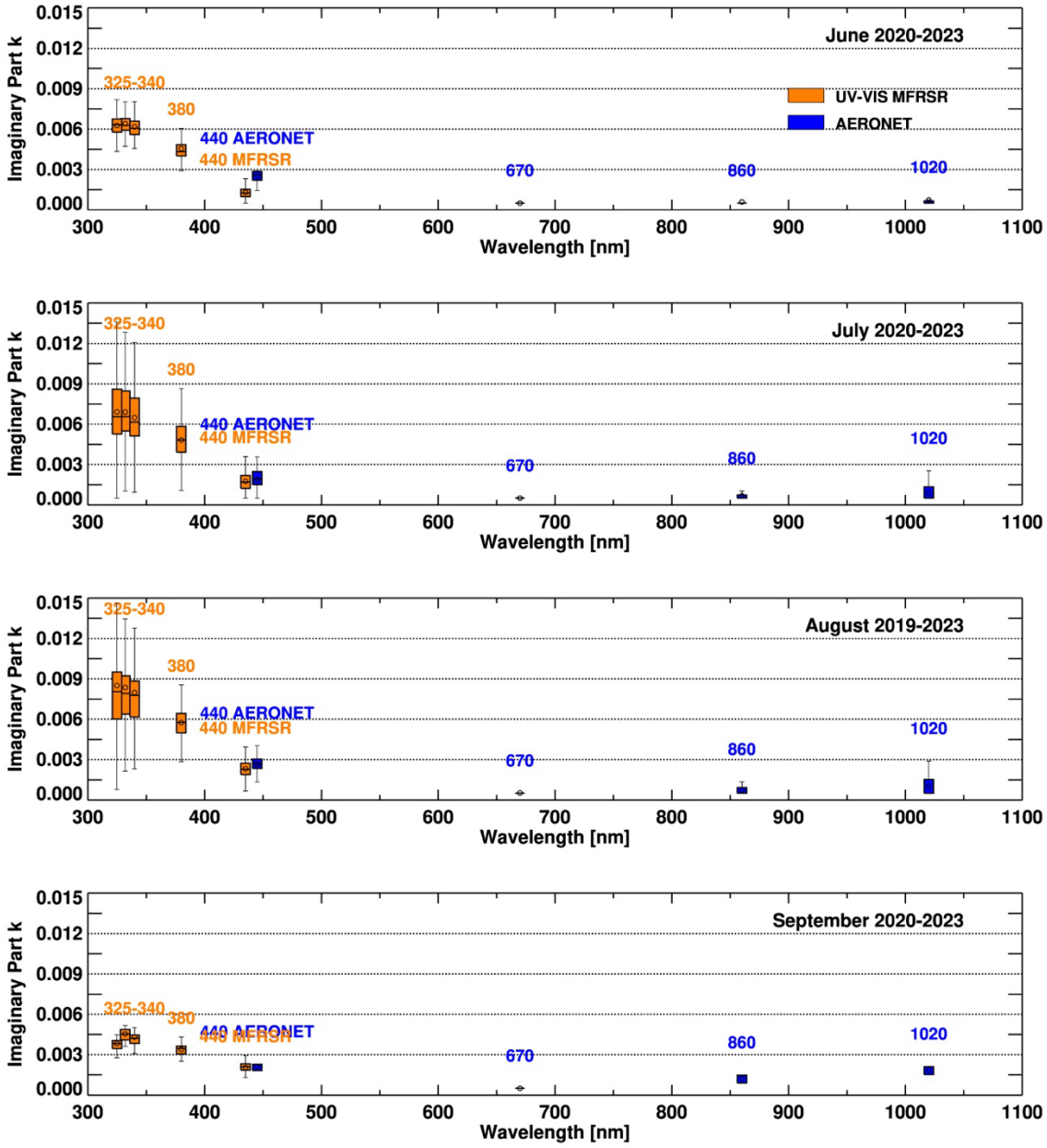

Figure 15. Spectral plots of the imaginary part of the refractive index retrieved from the MFRSR (325-440 nm) and AERONET (440-1020 nm) instruments. The spectral SSA dataset represents AE<0.6 and AOD_{440}>0.4 conditions and are shown as a box-whisker plot for each wavelength separately for the months of June, July, August, and September 2019-2023 in top to bottom order.

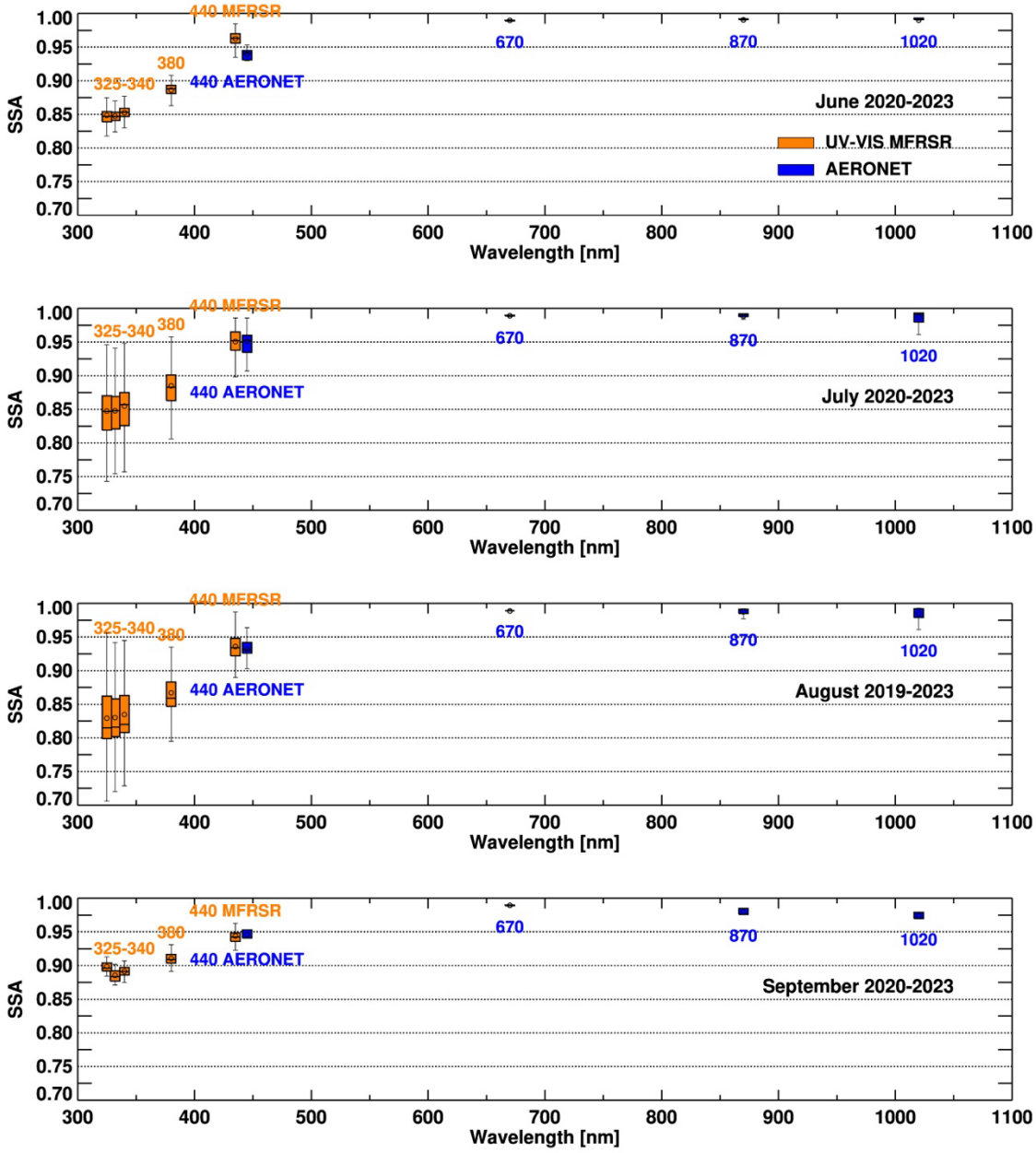

1165 **Figure 16.** Same as in Figure 15 but for the derived spectral SSA.

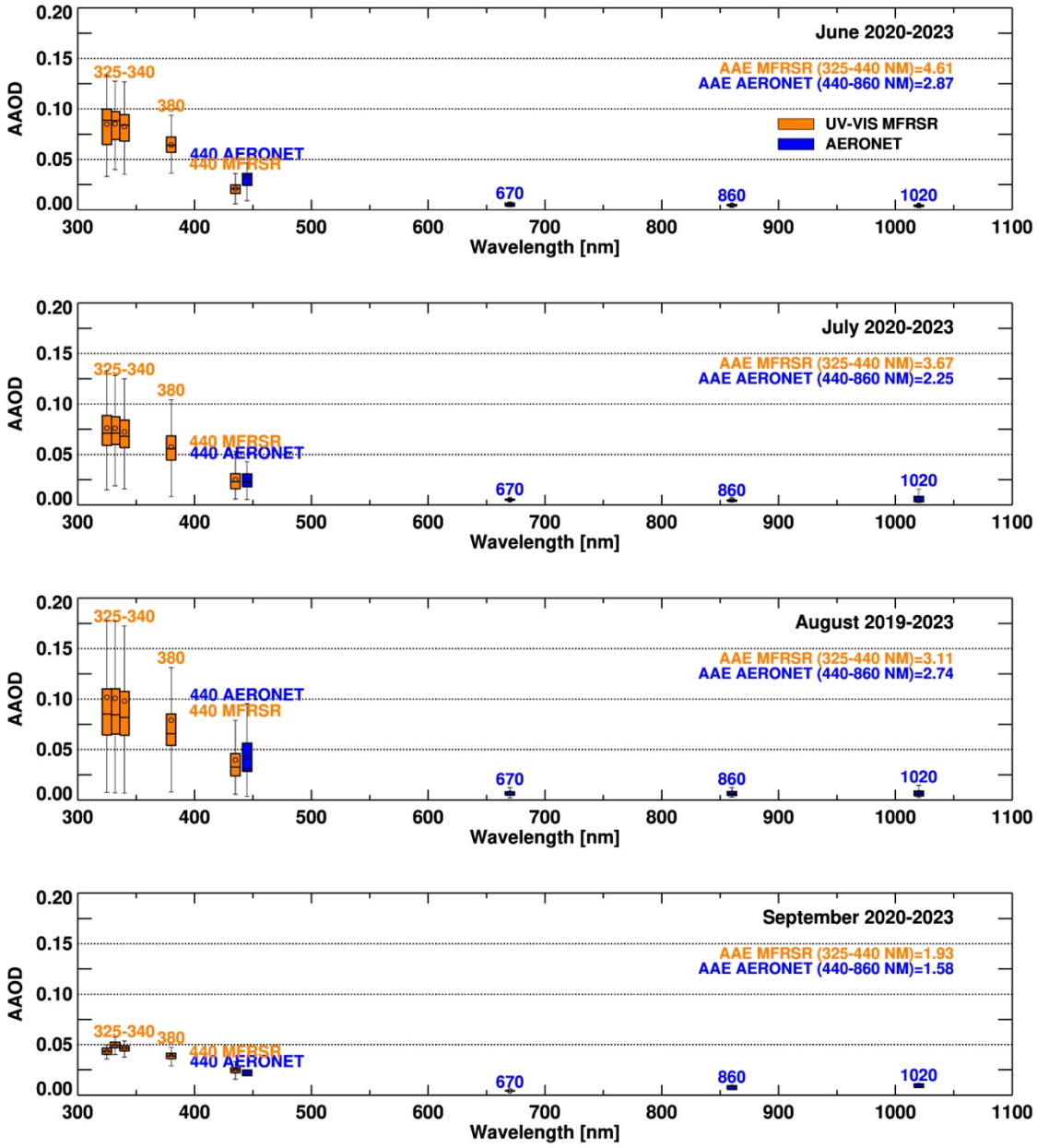

Figure 17. As in Figure 15 but for the derived spectral aerosol absorption optical depth (AAOD). The aerosol Absorption Ångström Exponent (AAE) values calculated separately for UV and VIS-NIR wavelength ranges are also included in each AAOD plot.